Monthly Notices of the ROYAL ASTRONOMICAL SOCIETY

MNRAS **526,** 2086–2103 (2023) https://doi.org/10.1093/mnras/stad2889
Advance Access publication 2023 September 22

Unveiling the accretion scenario of BH-ULXs using *XMM–Newton* observations

Seshadri Majumder [1★] Santabrata Das [1★] Vivek. K. Agrawal[2] and Anuj Nandi[2★]

[1]*Department of Physics, Indian Institute of Technology Guwahati, Guwahati 781039, India*
[2]*Space Astronomy Group, ISITE Campus, U. R. Rao Satellite Centre, Outer Ring Road, Marathahalli, Bangalore 560037, India*

Accepted 2023 September 20. Received 2023 September 20; in original form 2023 February 24

ABSTRACT

We present a comprehensive spectrotemporal analysis of five ultraluminous X-ray sources (ULXs) with central object likely being a black hole, using archival *XMM–Newton* observations. These sources, namely NGC1313 X−1, NGC5408 X-1, NGC6946 X−1, M82 X−1, and IC342 X−1, reveal short-term variability with fractional variance of 1.42−27.28 per cent and exhibit Quasi-periodic Oscillations (QPOs) with frequency $\nu_{\rm QPO} \sim 8-667$ mHz. Long-term evolution of ULXs energy spectra (0.3–10 keV; excluding M82 X−1) are described satisfactorily with a model combination that comprises a thermal Comptonization component (`nthComp`, yielding $\Gamma_{\rm nth} \sim 1.48$–$2.65$, $kT_{\rm e} \sim 1.62$–3.76 keV, $\tau \sim 8$–20, y-par$\sim$1.16–6.24) along with a standard disc component (`diskbb`, $kT_{\rm in} \sim 0.16$–0.54 keV). We find that these ULXs generally demonstrate anticorrelation between disc luminosity and inner disc temperature as $L_{\rm disc} \propto T_{\rm in}^{\alpha}$, where $\alpha = -3.58 \pm 0.04$ for NGC1313 X−1 and IC342 X−1, $\alpha = -8.93 \pm 0.11$ for NGC6946 X−1, and $\alpha = -10.31 \pm 0.10$ for NGC5408 X−1. We also obtain a linear correlation between bolometric luminosity $L_{\rm bol}$ and $\Gamma_{\rm nth}$ that indicates spectral softening of the sources when $L_{\rm bol}$ increases. We observe that in presence of QPO, Comptonized seed photon fraction varies in between $\sim 5-20$ per cent, while the Comptonized flux contribution (50−90 per cent) dominates over disc flux. Utilizing $\nu_{\rm QPO}$ and $L_{\rm bol}$, we constrain ULXs mass by varying their spin ($a_{\rm k}$) and accretion rate ($\dot{m}$). We find that NGC6946 X−1 and NGC5408 X−1 seem to accrete at sub-Eddington accretion rate provided their central sources are rapidly rotating, whereas IC342 X−1 and NGC1313 X−1 can accrete in sub/super-Eddington limit irrespective to their spin values.

Key words: accretion, accretion disc – black hole physics – radiation mechanisms: general – stars: individual: NGC1313 X−1, NGC5408 X−1, NGC6946 X−1, M82 X−1, IC342 X−1 – X-rays: galaxies.

1 INTRODUCTION

Ultraluminous X-ray sources (ULXs) are the bright off-nuclear point objects having luminosity in excess of Eddington luminosity ($\sim 10^{39}$ erg s^{-1} for 10M$_{\odot}$ object; Fabbiano 1989; Makishima et al. 2000). In general, the luminosities of these objects are found to lie in the range of 10^{39}–10^{41} erg s^{-1} (Fabbiano 1989; Feng & Soria 2011). Interestingly, the exact nature of the central accretor in ULXs as well as the plausible mechanisms to produce such a high luminosity still remain elusive (Fabrika et al. 2021, for a recent review). Meanwhile, several attempts were made to infer the characteristics of the ULXs. In an earlier attempt, it was indicated that the ULXs possibly harbour the stellar mass black hole (StMBH) that presumably accretes at super-Eddington rate (Fabrika & Mescheryakov 2001; Watarai, Mizuno & Mineshige 2001; Ebisawa et al. 2003; Poutanen et al. 2007, and references therein). The alternative explanation rely on the fact that sub-Eddington accretion onto the intermediate mass black holes (IMBHs) of mass 10^3–$10^5 M_{\odot}$ seems to power the ULXs (Colbert & Mushotzky 1999; Makishima et al. 2000; Miller et al. 2003). In addition, the possibility of harbouring magnetized neutron star in ULXs is discussed to explain the discovery of coherent pulsation in M82 X−2 (Bachetti et al. 2014) followed by other such sources (Fürst et al. 2016; Israel et al. 2017; Carpano et al. 2018; Sathyaprakash et al. 2019; Rodríguez Castillo et al. 2020; Quintin et al. 2021, and references therein). An alternative scenario based on the sub-Eddington accretion onto StMBHs with beamed emission is also propounded (Reynolds et al. 1997; King 2002), however it suffers lack of observational support (Feng & Soria 2011). Needless to mention that all the above efforts fail to converge in explaining the nature of the central accreter as well as the environment of the ULXs and hence remain under debate.

Interestingly, in the quest of ULXs, the study of the short-term variability including quasi-periodic oscillations (QPOs) observed in the power density spectra (PDS) are believed to be a viable tool as it carries the imprint signatures of the accretion dynamics and the nature of the accreter. So far, a handful ULXs are found to exhibit QPOs, namely NGC 1313 X−1 (QPO frequency $\nu_{\rm QPO} \sim 290$ mHz; Pasham et al. 2015), (∼80, ∼268, and ∼297 mHz; Atapin, Fabrika & Caballero-García 2019), NGC 5408 X−1 (∼20 mHz; Strohmayer et al. 2007), (10−42 mHz; Strohmayer & Mushotzky 2010; Atapin et al. 2019), M82 X−1 (∼54 mHz; Strohmayer & Mushotzky 2003), (∼110 mHz; Dewangan, Titarchuk & Griffiths 2006), (∼46 mHz;

★ E-mail: sbdas@iitg.ac.in (SD); anuj@ursc.gov.in (AN); smajumder@iitg.ac.in (SM)

Caballero-García, Belloni & Zampieri 2013), (∼35 and ∼47 mHz; Atapin et al. 2019), NGC 6946 X−1 (∼8.5 mHz; Rao, Feng & Kaaret 2010), (Atapin et al. 2019; ∼9.4, ∼27, and ∼42 mHz), IC 342 X−1 (∼642 mHz; Agrawal & Nandi 2015). It may be noted that the characteristics of mHz QPOs resemble with the Type-C low frequency QPOs (LFQPOs) frequently observed in black hole X-ray binaries (BH-XRBs) (Belloni et al. 2005; Nandi et al. 2012; Sreehari et al. 2019, and references therein). Several studies indicate that the mass of ULXs can be determined from the appropriate scale factor corresponding to the QPO frequencies observed in BH-XRBs and ULXs, and eventually favours the existence of IMBH (Dewangan et al. 2006; Strohmayer & Mushotzky 2009; Feng, Rao & Kaaret 2010; Pasham & Strohmayer 2012; Agrawal & Nandi 2015). Further, using *RXTE* observations of M82 X−1, Pasham, Strohmayer & Mushotzky (2014) discovered a pair of coherent QPO frequency ∼3.32 and ∼5.07 Hz with the harmonic ratio 3:2. These QPOs can be interpreted as analogous to the high frequency QPO (HFQPO) often seen in several BH-XRBs (Belloni, Sanna & Méndez 2012; Sreehari et al. 2020; Majumder et al. 2022) and consequently, a $\sim 428 M_{\odot}$ black hole is expected to be present at the core of M82 X−1 (Pasham et al. 2014, 2015; Kaaret, Feng & Roberts 2017). Needless to mention that the estimation of source mass by means of QPO frequency is not always free from caveats (Middleton et al. 2011).

The study of ULXs spectra is carried out over the decades starting from *ASCA* mission (energy range below ∼10 keV) in late 1990s (Colbert & Mushotzky 1999). Later on, rigorous spectral studies were performed using the high quality spectra from *XMM-Newton*, *Chandra*, and *NuSTAR* observatories (Walton et al. 2018a, 2019, 2020; Gúrpide et al. 2021; Salvaggio et al. 2022, and references therein). In general, ULXs spectra show two common features: a spectral turnover below ∼10 keV and a soft excess below ∼2 keV (Stobbart, Roberts & Wilms 2006; Feng & Soria 2011; Ghosh, Rana & Bachetti 2022). Based on the observed spectral morphologies, the ULXs spectra are classified into three spectral regimes, namely the *broadened disc, hard-ultraluminous* state, and *soft-ultraluminous* state (Gladstone, Roberts & Done 2009; Sutton, Roberts & Middleton 2013). Meanwhile, spectral fitting of many ULXs with the empirical model combinations consisting of a standard accretion disc component and a Comptonization component indicates the presence of a cool inner accretion disc ($kT_{\rm in} \sim 0.1$–0.3 keV) and an optically thick ($kT_e \sim 1$–2 keV and $\tau > 6$) corona (Gladstone et al. 2009). The inferred inner disc temperature implies a compact object of mass $\sim 10^3 M_{\odot}$ (following $T_{\rm in} \propto M^{-0.25}$; Kaaret et al. 2017) that supports the IMBH interpretation with sub-Eddington accretion (Feng & Soria 2011). On the contrary, several ULXs are found to comply steep power law ($\Gamma \gtrsim 2.5$) dominated spectral states of StMBH accreting at near-Eddington rate (Feng & Kaaret 2005; Winter, Mushotzky & Reynolds 2006; Feng & Soria 2011).

Models of accretion disc have been adopted to delineate the ULX spectra where two disc blackbody like components with different temperatures were used (Stobbart et al. 2006; Poutanen et al. 2007; Kara et al. 2020). In these studies, it is suggested that the hotter component originates from the inner accretion flow by means of the inverse Comptonization of the soft photons by the swarm of hot electrons present in the corona (Roberts 2007; Middleton et al. 2015; Mukherjee et al. 2015; Jithesh, Misra & Wang 2017). On the contrary, the emission of the soft component is possibly emerged from the optically thick outflow originated within/from the spherization radius (Shakura & Sunyaev 1973; Poutanen et al. 2007). In addition, the slim disc model (Abramowicz et al. 1988) with varying radial temperature index is also found to be successful in describing the ULXs spectra (see Watarai et al. 2001; Miyawaki et al. 2006; Vierdayanti et al. 2006; Ghosh & Rana 2021). However, Gladstone et al. (2009) indicate that the slim disc model is perhaps inadequate in describing the spectra of ULXs resulting unphysical disc temperature ($kT_{\rm in} \gtrsim 3$ keV).

Indeed, some of the ULXs may harbour neutron star accretor although they do not display any pulsed emission (King, Lasota & Kluźniak 2017; Walton et al. 2018b). Meanwhile, piece-wise efforts were given in studying the temporal and spectral properties of the ULXs considering black hole accretor (hereafter BH-ULX) at its centre (Rao et al. 2010; Bachetti et al. 2013; De Marco et al. 2013; Marlowe et al. 2014; Agrawal & Nandi 2015; Stuchlík & Kološ 2015; Brightman et al. 2016b; Luangtip et al. 2021). Interestingly, some of the BH-ULXs are seen to exhibit QPO features, although their physical origin still remains elusive. Indeed, there are few occasions where combined spectrotemporal properties are studied to examine the characteristics of the BH-ULXs. Pasham & Strohmayer (2012) found nearly non-varying spectral properties in most of the observations of NGC 5408 X−1, that evidently suggest the absence of its correlation with the observed QPO frequency. Further, despite having the lack of statistical significance, Caballero-García et al. (2013) reported the decrease of $\nu_{\rm QPO}$ with the increase of Comptonized flux for M82 X−1, however, the origin of such correlation is poorly understood.

Considering all these, in this work, we aim to address the scarcity in understanding the accretion scenario of the BH-ULXs and perform the in-depth spectrotemporal analysis for these sources. Towards this, we revisit the archival *XMM–Newton* observations of the BH-ULXs that predominantly exhibit QPO features. While doing so, we investigate the fractional variability ($F_{\rm var}$) as well as the hardness intensity diagram (HID) in order to explain the variability properties of the source. We perform spectral modelling using the combined *XMM–Newton* data of *EPIC-PN* and *EPIC-MOS* instruments in 0.3–10 keV energy range with both phenomenological and physical models. We observe significant spectrotemporal correlations for four BH-ULXs under consideration. Further, following a novel formalism developed by Das et al. (2021), we estimate the possible mass ($M_{\rm BH}$) range of these BH-ULX sources by means of their spin ($a_{\rm k}$) and accretion rates ($\dot{m}$).

The paper is organized as follows. In Section 2, we present the selection criteria of the BH-ULXs and briefly mention the source characteristics. In Section 3, we discuss the data reduction procedure of *EPIC-PN* and *EPIC-MOS* instruments. We present the results from timing and spectral analyses in Sections 4 and 5, respectively. The spectrotemporal correlation results are studied in Section 6. In Section 7, we estimate the possible mass range of the BH-ULXs. Finally, we discuss the results and present conclusion in Section 8.

2 SOURCE SELECTION AND OBSERVATION

In this work, we analyse the *XMM–Newton* (Jansen et al. 2001) observations of the ULXs that exhibit QPO features. Accordingly, we select five ULXs, namely NGC 1313 X−1, NGC 5408 X−1, NGC 6946 X−1, M82 X−1, and IC 342 X−1, and use the archival data available in HEASARC public data base.[1] Here, we consider the ULXs harbouring black hole (BH-ULXs) at their central core and carry out the analyses.

We consider all observations of the chosen sources for examining the correlations among the spectrotemporal properties. Note that these sources were observed for multiple times in a given year, although they do not display significant spectrotemporal changes

[1] https://heasarc.gsfc.nasa.gov/db-perl/W3Browse/w3browse.pl

Table 1. Observation details of the five ULXs observed with *XMM–Newton*. In the table, source name, ObsID, Epoch, date of observation along with MJD, and exposure time are mentioned. The count rate in 0.3–10 keV energy range of the *EPIC-PN* detector along with hardness ratio (HR) and fractional variability ($F_{\rm var}$) in percentage are also tabulated. See the text for details.

Source	ObsID	Epoch$^{\otimes}$	Date	MJD	Effective exposure (ks)	Rate (cts s^{-1}) (0.3–10 keV)	HR (C_2/C_1)*	($F_{\rm var}$)$^{\boxtimes}$ (per cent)
NGC 1313 X-1	0106860101†	XM1	2000-10-17	51834.14	10.6	0.85 ± 0.08	0.38 ± 0.08	3.63 ± 1.16
	0205230601†	XM2	2005-02-07	53408.48	8.2	1.01 ± 0.10	0.37 ± 0.09	3.30 ± 1.43
	0 405 090 101	XM3	2006-10-15	54023.98	38.0	0.85 ± 0.08	0.39 ± 0.08	3.48 ± 2.27
	0 693 850 501	XM4	2012-12-16	56277.67	32.4	1.03 ± 0.08	0.36 ± 0.07	3.36 ± 1.79
	0 693 851 201	XM5	2012-12-22	56283.66	63.7	1.08 ± 0.05	0.27 ± 0.05	1.54 ± 0.15
	0742590301†	XM6	2014-07-05	56843.97	60.0	1.81 ± 0.11	0.34 ± 0.05	4.17 ± 1.04
	0742490101†	XM7	2015-03-30	57111.19	63.8	0.86 ± 0.09	0.40 ± 0.09	2.43 ± 0.47
	0803990101†	XM8	2017-06-14	57918.89	132.2	1.70 ± 0.11	0.36 ± 0.05	27.28 ± 0.26
	0803990301†	XM9	2017-08-31	57996.68	33.8	0.93 ± 0.08	0.39 ± 0.08	2.75 ± 2.57
	0803990601†	XM10	2017-12-09	58096.46	33.6	1.73 ± 0.11	0.33 ± 0.05	2.84 ± 1.29
NGC 5408 X-1	0112290501†	XM1	2001-07-31	52121.54	3.0	1.53 ± 0.11	0.05 ± 0.02	7.63 ± 0.19
	0112291001†	XM2	2002-07-29	52484.35	6.0	1.19 ± 0.12	0.15 ± 0.05	12.09 ± 0.35
	0112291201†	XM3	2003-01-27	52667.01	2.8	0.95 ± 0.08	0.08 ± 0.03	16.23 ± 0.12
	0 302 900 101	XM4	2006-01-13	53748.77	81.2	1.08 ± 0.05	0.07 ± 0.02	9.12 ± 1.01
	0 500 750 101	XM5	2008-01-13	54478.79	34.1	0.99 ± 0.05	0.08 ± 0.03	12.35 ± 0.53
	0 653 380 201	XM6	2010-07-17	55394.13	77.3	1.22 ± 0.06	0.08 ± 0.03	7.29 ± 1.11
	0 653 380 301	XM7	2010-07-19	55396.13	89.4	1.20 ± 0.06	0.08 ± 0.02	6.12 ± 1.39
	0 653 380 401	XM8	2011-01-26	55587.67	80.5	1.14 ± 0.06	0.09 ± 0.02	6.87 ± 1.31
	0 653 380 501	XM9	2011-01-28	55589.65	46.5	1.08 ± 0.05	0.09 ± 0.03	7.45 ± 0.94
	0 723 130 301	XM10	2014-02-11	56699.02	18.7	0.99 ± 0.02	0.10 ± 0.03	10.33 ± 0.46
	0 723 130 401	XM11	2014-02-13	56701.02	33.1	1.08 ± 0.08	0.10 ± 0.02	11.02 ± 0.52
NGC 6946 X-1	0 200 670 301	XM1	2004-06-13	53169.78	9.7	0.39 ± 0.05	0.16 ± 0.06	14.61 ± 0.65
	0 500 730 201	XM2	2007-11-02	54406.91	31.6	0.37 ± 0.06	0.17 ± 0.07	21.92 ± 0.91
	0 500 730 101	XM3	2007-11-08	54412.94	18.5	0.38 ± 0.06	0.18 ± 0.08	26.96 ± 0.74
	0 691 570 101	XM4	2012-10-21	56221.74	56.8	0.44 ± 0.06	0.19 ± 0.07	7.35 ± 2.59
	0870830101†	XM5	2020-07-08	59038.93	12.6	0.42 ± 0.08	0.18 ± 0.05	24.52 ± 2.26
	0870830201†	XM6	2020-12-15	59198.32	16.1	0.37 ± 0.11	0.19 ± 0.06	7.10 ± 1.22
	0870830301†	XM7	2021-04-04	59308.22	10.7	0.38 ± 0.06	0.19 ± 0.08	13.30 ± 0.89
	0870830401†	XM8	2021-05-25	59359.89	12.5	0.34 ± 0.05	0.19 ± 0.09	23.82 ± 0.55
M82 X-1	0 112 290 201	XM1	2001-05-06	52035.38	15.2	4.17 ± 0.18	1.08 ± 0.09	2.99 ± 0.37
	0 206 080 101	XM2	2004-04-21	53116.90	29.0	3.17 ± 0.16	0.65 ± 0.07	1.42 ± 0.48
	0560590101†	XM3	2008-10-03	54742.88	19.2	8.01 ± 0.27	1.40 ± 0.10	8.87 ± 0.16
	0560590301†	XM4	2009-04-29	54950.36	15.2	4.91 ± 0.20	0.90 ± 0.07	2.51 ± 0.40
	0 657 800 101	XM5	2011-03-18	55638.69	9.2	3.24 ± 0.22	0.83 ± 0.05	8.77 ± 0.87
	0 657 801 901	XM6	2011-04-29	55680.55	3.9	3.05 ± 0.15	0.59 ± 0.06	3.03 ± 0.26
	0 657 802 101	XM7	2011-09-24	55828.21	10.5	3.19 ± 0.16	1.00 ± 0.09	3.10 ± 0.41
IC 342 X-1	0093640901†	XM1	2001-02-11	51951.06	5.4	0.47 ± 0.06	1.03 ± 0.30	3.44 ± 1.89
	0206890101†	XM2	2004-02-20	53055.31	6.6	0.98 ± 0.09	0.94 ± 0.18	2.45 ± 1.49
	0206890201†	XM3	2004-08-17	53234.82	19.6	0.55 ± 0.07	0.94 ± 0.24	6.42 ± 1.64
	0 693 850 601	XM4	2012-08-11	56150.83	36.0	0.52 ± 0.06	0.97 ± 0.24	3.85 ± 3.58
	0693851301†	XM5	2012-08-17	56156.84	37.4	0.66 ± 0.07	0.91 ± 0.19	2.27 ± 4.39

Notes. $^*C_1$ and C_2 are the count rates in 0.3–2 keV and 2–10 keV energy ranges, respectively.
†Non-detection of QPO.
$^{\boxtimes}$Fractional variability, calculated from the background subtracted *EPIC-PN* light curves in 0.3–10 keV energy range.
$^{\otimes}$XM*i* stands for *XMM–Newton*, where *i* can run from 1 to 11 based on the observations.

in their characteristics. Hence, we consider only those observations which are typically separated by about six months interval to avoid repetition of results. Further, we consider three observations for NGC 1313 X−1 as it was observed six times in 2017 (Walton et al. 2020). All the selected observations under consideration are listed in Table 1. We present brief description of the selected sources below.

2.1 NGC 1313 X−1

NGC 1313 X−1 is one of the three bright ULXs located in the nearby ($d \sim 4.25$ Mpc) barred spiral galaxy NGC 1313 (Tully, Courtois & Sorce 2016). The source luminosity is observed as $\sim 10^{40}$ erg s^{-1}. The source belongs to the hard-ultraluminous spectral state and exhibits significant spectral variability (Pintore & Zampieri 2012). It is suggested that the source is powered by the super-Eddington accretion onto stellar-mass black hole (Gladstone et al. 2009; Bachetti et al. 2013). On the contrary, the sub-Eddington accretion on to IMBH of mass 2524–6811$M_{\odot}$ is also believed to be an alternative possibility (Huang 2019). The spin ($a_{\rm k}$) of the source is reported as 0.960–0.998 (Caballero-García & Fabian 2010), indicating a maximally rotating BH-ULXs.

2.2 NGC 5408 X−1

NGC 5408 X−1 is a nearby ULX source at a distance of 4.8 Mpc, located at ∼20 arcsec off from the centre of the host galaxy NGC 5408 (Luangtip et al. 2021). The observed peak luminosity is found as $\sim 10^{40}$ erg s^{-1}. The source is a good candidate for the timing studies as it exhibits variabilities on different time-scales ranging from few tens of seconds to few months (Strohmayer 2009; Heil & Vaughan 2010; De Marco et al. 2013; Hernández-García et al. 2015). Employing the scaling law of QPO frequency as well as the dynamical mass measurement, the mass of the central source is obtained within IMBH regime (Strohmayer & Mushotzky 2009; Cseh et al. 2013; De Marco et al. 2013; Luangtip et al. 2021). Using reflection spectroscopy, Caballero-García & Fabian (2010) reported the spin of the source as $0.70^{+0.12}_{-0.05}$.

2.3 NGC 6946 X−1

NGC 6946 X−1 is one of the four ULXs in the spiral galaxy NGC 6946 at a distance of 7.72 Mpc (Anand, Rizzi & Tully 2018). This source is found to be one of the most variable ULXs that demonstrates short term variabilities with fractional rms amplitude reaching up to ∼ 60 per cent (Rao et al. 2010). In addition, the existence of soft lag at the lower frequencies and hard lag at relatively higher frequencies are reported (Hernández-García et al. 2015). Upon scaling the mHz QPO frequency detected for this source with the low frequency QPOs (LFQPOs) of the galactic BH-XRBs, the mass of NGC 6946 X−1 is revealed as (1–4) × 10^3 $M_\odot$ (Rao et al. 2010). It is noteworthy to mention that the spin of the central source in NGC 6946 X−1 remains inconclusive till date.

2.4 M82 X−1

The 'cigar galaxy' commonly known as M82 resides at a distance of 3.63 Mpc (Middleton et al. 2015) and hosts two well-known ULX sources M82 X−1 and X−2 separated by only 5 arcsec (Brightman et al. 2020) in the sky plane. M82 X−1, being the most luminous ULX of the host galaxy with peak luminosity reaching up to $\sim 10^{41}$ erg s^{-1}, remains one of the most promising IMBH candidate over the years. The mass of M82 X−1 is predicted as 300–810$M_\odot$ from the mass–luminosity correlation (Feng et al. 2010), although Pasham et al. (2014) inferred its mass as ∼400$M_\odot$ from the scaling relation of 3:2 twin-peaked QPO frequency. Further, Stuchlík & Kološ (2015) reported the ranges of mass and spin of the source as $140M_\odot < M_{\rm BH} < 660M_\odot$ and $0.05 < a_{\rm k} < 0.6$, respectively.

2.5 IC 342 X−1

IC 342 is a nearby spiral galaxy at a distance ∼3.61 Mpc (Middleton et al. 2015) and it contains two ULXs, namely IC 342 X−1 and X−2. The source IC 342 X−1 is one of the most studied ULX sources since its discovery by *Einstein* IPC observations (Fabbiano & Trinchieri 1987). Subsequently, *ROSAT* (Bregman, Cox & Tomisaka 1993; Roberts & Warwick 2000) and *ASCA* observations (Kubota et al. 2001) also confirmed its ultraluminous state with maximum observed luminosity $\gtrsim 10^{39}$ erg s^{-1}. The spectral state transitions, namely from the disc-dominated state to the power-law dominated state, are first observed in IC 342 X−1 (Kubota et al. 2001). Several studies from observational and theoretical fronts predict the mass of IC 342 X−1 in the range of 20–1783 $M_\odot$ (Marlowe et al. 2014; Agrawal & Nandi 2015; Das et al. 2021). Moreover, the spinning nature of the source still remains inconclusive.

3 DATA REDUCTION

We follow the standard data reduction procedure[2] using the software `SCIENCE ANALYSIS SYSTEM (SAS) V19.1.0`[3] of *XMM–Newton* instrument. Note that the data of all the observations are available in *PrimeFullWindow* mode for the sources under consideration. For spectral analysis, we use combined *EPIC-PN* (Strüder et al. 2001) and *EPIC-MOS* data, whereas the timing analysis is carried out using *EPIC-PN* data due to better timing resolution (∼73.4 ms) of the instrument. The event files are generated using the standard task `epchain` and `emproc` for *EPIC-PN* and *EPIC-MOS*, respectively. First, we generate a light curve in 10–15 keV energy range to identify the effect of particle background flares in the observations. Following Agrawal & Nandi (2015), the Good Time Intervals (GTIs) are generated using the task `tabgtigen` by adopting the selection criteria `RATE` ≤3 × mean count rate of the light curve in 10–15 keV energy range. The above selection criteria removes all the background flares including data gaps in the light curves. We consider data corresponding to the longest continuous observation available in the GTI segments. Finally, the cleaned event file is generated using the selected GTI interval to extract the science products. The events are selected according to the selection criteria `PATTERN` ≤4 and `PATTERN` ≤12 with `FLAG`=0 for *EPIC-PN* and *EPIC-MOS*, respectively. The task `evselect` is used to generate light curves which are further corrected with background subtraction and various instrumental effects, such as vignetting, bad pixels using the tool `epiclccorr`. The source and background spectra are extracted using the task `evselect`. Instrument response file (rmf) and ancillary response file (arf) are generated using the tasks `rmfgen` and `arfgen`, respectively.

Following Kajava & Poutanen (2009) and Agrawal & Nandi (2015), light curves and spectra are extracted from a 40 arcsec circular region concentric with the source coordinate for all the sources except M82 X−1 and NGC 6946 X−1. However, the source region is reduced to 30 arcsec in few of the observations including NGC 6946 X−1, provided the source falls near the chip gap of pn camera. A smaller circular source region of 18 arcsec is chosen for M82 X−1 to minimize the chance of contamination from nearby sources (Dewangan et al. 2006). Backgrounds are estimated by extracting the counts from the identical circular region resides away from the source.

4 TIMING ANALYSIS AND RESULTS

Here, we explore the temporal variabilities of five BH-ULXs under considerations and the obtained results are presented in the subsequent sections.

4.1 Variability and hardness-intensity diagram (HID)

We study the short-term variability of five BH-ULXs under consideration. While doing so, background subtracted 200 s binned *EPIC-PN* light curves are generated for each of the sources in 0.3–10 keV energy range. We compute the fractional variability ($F_{\rm var}$) i.e. the rms variability amplitude normalized to mean count rate (Edelson et al. 2002; Vaughan et al. 2003; Pintore et al. 2014; Bhuvana et al. 2021) in 0.3–10 keV energy range to deduce the variability of the sources in the time domain. The fractional variabilities of all five sources are found to vary in the range of 1.42–27.28 per cent, whereas NGC

[2]https://www.cosmos.esa.int/web/xmm-newton/sas-threads
[3]https://www.cosmos.esa.int/web/xmm-newton/sas

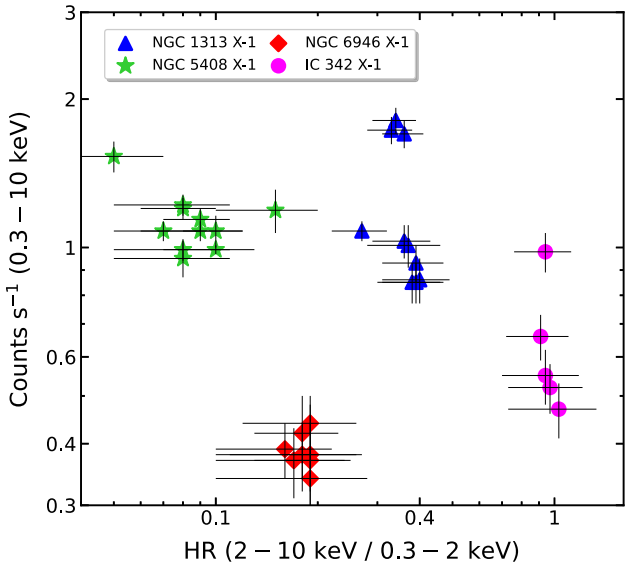

Figure 1. HID of the BH-ULXs. The variation of *EPIC-PN* background subtracted count rate in 0.3–10 keV energy range with the hardness ratio is shown for each source. See the text for details.

6946 X−1 is appeared to be most variable with $F_{\rm var} \sim 27$ per cent. The mean count rate and the fractional variability corresponding to each observations are tabulated in Table 1.

Further, we study the HID of the four BH-ULXs. The hardness ratio is defined as HR = C2/C1, where C1 and C2 are the background subtracted count rates in 0.3–2 keV and 2–10 keV energy bands, respectively. It may be noted that the soft energy band is considered up to ∼2 keV as the disc emission generally dominates within this energy range for ULXs (see Section 5). The obtained HR values are mentioned in Table 1 for all the observations. In Fig. 1, we present the HID of the four BH-ULXs, where source count rate is plotted with HR in logarithmic scales. In the HID plot, results corresponding to various sources are presented using different point styles as shown in the legend. We observe that the intensity of NGC 5408 X−1 noticeably varies with HR, although the change of HR seems to be marginal for other three sources.

4.2 Power spectral properties

We generate PDS for all the observations using the *EPIC-PN* data in 0.3–10 keV energy range. The ftools task `powspec`[4] available in `HEASOFT V6.29.1`[5] is used to obtain the PDS. Background subtracted light curves of 0.5 s time resolution are used to generate the PDS with Nyquist frequency of 1 Hz. In general, the light curves are divided into shorter segments of equal duration to generate individual power spectrum. All the power spectra are further averaged in a single frame to obtain the resultant PDS. We notice that the number of newbins per interval (in `powspec`), which determines the duration of the light-curve segments, plays an important role in order to maximize the signal-to-noise ratio in the power spectra. In particular, we observe that the specific choice of the number of newbins per interval results the prominent feature of individual QPOs provided the minimum frequency in the PDS is chosen as roughly one-tenth to one-thirtieth of the observed QPO frequency. A similar method is adopted in Atapin et al. (2019) to obtain the PDS of the sources under consideration. We choose specific number of newbins per interval (see Table. 2) to construct the individual PDS, which is further averaged in a single frame to obtain the resultant PDS for the significant detection of QPO features. A constant binning factor of 1.04 is used to rebin the final PDS in the frequency space. Note that the number of newbins per interval plays an important role in order to maximize the signal-to-noise ratio in the power spectra to detect the prominent QPO features. The number of newbins per interval is presented in Table 2.

Each PDS expressed in Leahy normalization (Leahy et al. 1983) represents a Poisson noise of power level ∼2 with flat-topped noise (FTN) at the low frequency along with QPO features. Following Caballero-García et al. (2013), we adopt the model combination comprising of a `constant` (for the Poisson noise power), zero centroid `Lorentzian` (for the low frequency FTN), and an additional `Lorentzian` profile (for the QPO feature) to obtain the best-fitting power spectra. Each Lorentzian is characterized by three parameters, namely centroid (LC), width (LW), and normalization (LN) (see Sreehari et al. 2020; Majumder et al. 2022, and references therein). The model fitted PDS of five sources are depicted in the respective panels of Fig. 2. In the top panel, we display the power spectrum of NGC 5408 X−1 (ObsID−0653380201), where the Poisson noise level and the FTN are fitted with a `constant` and a zero centroid `Lorentzian` component. Next, we include one `Lorentzian` at ∼40 mHz to fit the excess positive residuals near this frequency. The fit is obtained with a $\chi^2_{\rm red}$ of 219/250 = 0.88, although significant positive residuals still remain around ∼100 mHz. To address this, another `Lorentzian` is added to the composite model at around ∼100 mHz. The resultant fit is obtained with a $\chi^2_{\rm red} = 0.85$. We follow the above methodology to fit all the remaining PDS corresponding to each source and find that the requirement of the number of model components generally vary with observations. It is perceived that the FTN in the PDS can be well-fitted using the zero centroid Lorentzian of all the sources except IC 342 X−1. A power-law profile with index ∼0.73 provides a better fit of the low frequency FTN component of IC 342 X−1.

The best-fitting PDS of NGC 5408 X−1 (ObsID−0653380201) confirms simultaneous detection of two QPOs at $\sim 38.13^{+0.28}_{-0.50}$ and $\sim 97.94^{+2.76}_{-2.72}$ mHz, respectively. The significance ($\sigma = LN/{\rm err}_{\rm neg}$, where $\rm err_{neg}$ being the negative error of normalization of the fitted `Lorentzian`) of the detected QPOs are obtained as 4.02σ and 2.73σ. The percentage rms amplitudes of ∼38.13 and ∼97.94 mHz QPOs are estimated (Sreehari et al. 2020; Majumder et al. 2022, and references therein) as 12.27 ± 1.19 per cent and 6.16 ± 0.48 per cent, respectively. Further, we calculate the rms amplitudes of the entire PDS in 0.001–1 Hz frequency range which is obtained as 31.40 ± 3.47 per cent. Following the above approach, we find the presence of QPO features in twenty one observations for all BH-ULXs and two of them exhibit twin peak QPO features (for NGC 1313 X−1 and NGC 5408 X−1, the $\nu_{\rm QPO} \sim 667$ and ∼98 mHz) that appear simultaneously in the PDS. The model fitted parameters and the estimated parameters of the QPO features are presented in Table 2.

5 SPECTRAL ANALYSIS AND RESULTS

We generate *XMM–Newton* energy spectra for all the observations in 0.3–10 keV energy range. `XSPEC V12.12.1f` (Arnaud 1996) of `HEASOFT V6.29.1` is used to model the energy spectrum. While spectral fitting, we follow the standard procedure to extract

[4]https://heasarc.gsfc.nasa.gov/xanadu/xronos/examples/powspec.html
[5]https://heasarc.gsfc.nasa.gov/xanadu/xspec/

Table 2. Details of the QPO characteristics obtained from the best-fitted PDS of five BH-ULXs in 0.3–10 keV energy range. Here, $\nu_{\rm QPO}$, FWHM, Q-factor, and σ denote the centroid frequency, width, quality factor, and significance of the QPO features. $\rm QPO_{rms}$ per cent and $\rm Total_{rms}$ per cent denote the percentage rms amplitudes of the QPOs and the entire PDS, respectively. All the errors are computed with 68 per cent confidence level. See the text for details.

Source	ObsID	MJD	$\nu_{\rm QPO}$ (mHz)	FWHM (mHz)	Q-factor$^{\boxtimes}$	Significance (σ)	$\rm QPO_{rms}$ (per cent)	$\rm Total_{rms}$ (per cent)	χ^2/dof	No. of Newbins per Interval
NGC 1313 X-1	0 405 090 101	54023.98	$82.14^{+1.35}_{-1.58}$	$9.12^{+4.64}_{-6.77}$	9.01	3.34	8.17 ± 0.49	22.59 ± 1.27	107/122	256
	0 693 850 501	56277.67	$304.60^{+4.21}_{-4.99}$	$33.34^{+11.12}_{-11.05}$	9.14	4.67	11.29 ± 0.59	18.74 ± 1.54	16/36	512
			$667.31^{+37.60}_{-47.19}$	$68.63^{+33.14}_{-22.58}$	9.72	1.62	7.04 ± 0.18	18.74 ± 1.54	16/36	512
	0 693 851 201	56283.66	$305.04^{+6.22}_{-3.58}$	$37.25^{+15.23}_{-10.18}$	8.18	2.76	11.46 ± 0.72	15.69 ± 0.95	51/50	256
NGC 5408 X-1	0 302 900 101	53748.77	$18.51^{+1.06}_{-1.14}$	$15.66^{+2.83}_{-2.43}$	1.18	9.41	15.37 ± 1.24	27.17 ± 10.84	542/506	1024
	0 500 750 101	54478.79	$9.02^{+0.67}_{-0.71}$	$2.56^{+2.45}_{-2.08}$	3.52	2.41	7.81 ± 2.62	28.97 ± 12.90	1225/1018	2048
	0 653 380 201	55394.13	$38.13^{+0.28}_{-0.50}$	$25.07^{+1.41}_{-1.19}$	1.52	4.02	12.27 ± 1.19	31.40 ± 3.47	210/247	512
			$97.94^{+2.76}_{-2.72}$	$10.79^{+0.74}_{-0.48}$	9.08	2.73	6.16 ± 0.48	31.40 ± 3.47	210/247	512
	0 653 380 301	55396.13	$39.14^{+0.27}_{-0.23}$	$6.54^{+0.62}_{-0.50}$	6.08	1.94	4.89 ± 0.50	23.54 ± 2.46	76/58	256
	0 653 380 501	55589.65	$17.99^{+1.58}_{-1.93}$	$14.31^{+4.41}_{-3.81}$	1.26	5.40	14.34 ± 1.81	28.33 ± 8.09	505/506	1024
	0 723 130 301	56699.02	$11.09^{+0.91}_{-1.04}$	$6.68^{+3.36}_{-2.74}$	1.66	3.51	13.92 ± 4.23	34.90 ± 9.10	33/40	256
			$44.22^{+1.84}_{-1.12}$	$3.87^{+3.05}_{-2.79}$	11.44	2.38	7.41 ± 1.41	34.90 ± 9.10	33/40	256
	0 723 130 401	56701.02	$13.08^{+0.74}_{-0.85}$	$7.39^{+3.44}_{-2.47}$	1.77	4.48	14.42 ± 3.98	32.10 ± 11.65	566/506	1024
NGC 6946 X-1	0 200 670 301	53169.78	$38.71^{+5.61}_{-2.53}$	$9.67^{+6.22}_{-5.84}$	4.00	2.04	29.05 ± 0.51	48.98 ± 6.01	149/122	512
	0 500 730 201	54406.91	$9.23^{+0.81}_{-0.92}$	$5.85^{+2.43}_{-2.02}$	1.59	3.79	20.60 ± 2.06	44.18 ± 12.32	1168/1018	2048
	0 500 730 101	54412.94	$8.44^{+0.43}_{-0.35}$	$1.91^{+1.19}_{-1.12}$	4.40	2.90	13.41 ± 2.13	38.35 ± 8.58	62/74	1024
	0 691 570 101	56221.74	$41.72^{+5.04}_{-5.69}$	$41.12^{+12.52}_{-13.09}$	1.01	4.32	23.47 ± 0.61	41.13 ± 2.74	133/122	256
M82 X−1 $^{\otimes}$	0 112 290 201	52035.38	$55.85^{+1.44}_{-2.01}$	$6.44^{+5.89}_{-3.45}$	8.67	2.37	11.54 ± 4.33	32.68 ± 10.30	637/506	2048
	0 206 080 101	53116.90	$110.81^{+5.03}_{-4.26}$	$31.82^{+19.72}_{-13.47}$	3.48	3.61	12.13 ± 2.18	20.21 ± 4.06	80/105	512
	0 657 800 101	55638.69	$45.55^{+1.61}_{-2.19}$	$5.85^{+4.41}_{-2.73}$	7.78	2.21	21.88 ± 7.75	68.48 ± 12.84	635/504	2048
	0 657 801 901	55680.55	$47.63^{+5.47}_{-3.22}$	$17.13^{+6.32}_{-5.28}$	2.78	2.94	32.95 ± 11.18	64.62 ± 24.32	362/250	512
	0 657 802 101	55828.21	$35.74^{+2.53}_{-2.44}$	$11.48^{+5.05}_{-3.73}$	3.12	3.33	28.30 ± 10.64	42.74 ± 14.28	53/58	1024
IC 342 X-1	0 693 850 601	56150.83	$643.40^{+15.30}_{-23.89}$	$112.20^{+59.69}_{-46.52}$	5.73	3.75	25.82 ± 0.46	48.30 ± 13.74	32/51	256

Notes. $^{\boxtimes}Q \lesssim 2$ indicates 'QPO like' broad features (van der Klis 2006, for detail).
$^{\otimes}$Estimated $\rm QPO_{rms}$ per cent considering possible flux contamination due to M82 X−2 (see Appendix-A for details).

the background spectrum file, instrument response file (rmf), and ancillary response file (arf). Each spectrum is grouped with 25 counts per spectral bin using `specgroup` tool of `SAS V19.1.0`. We fit *EPIC-PN* and *EPIC-MOS* spectra simultaneously to improve the counting statistics. The cross-calibration between different instruments is taken care by including a `constant` component in the spectral fitting (Pintore et al. 2014). For NGC 5408 X−1, we include a plasma component (`APEC` in `XSPEC`) of temperature ∼0.9 keV to adjust the low energy residuals (see Pintore et al. 2014). Following Earnshaw et al. (2019), we include a `gaussian` at ∼1 keV to fit the NGC 6946 X−1 spectra. We do not include M82 X−1 in the spectral study as the effect of contamination due to the close proximity (within 5 arcsec) of M82 X−2 cannot be ruled out (Brightman et al. 2016a).

5.1 Modelling of *XMM–Newton* spectra

We initially model the energy spectra of *XMM–Newton* in 0.3–10 keV energy range using the phenomenological model combination `TBabs×(diskbb + diskbb)`. Here, `TBabs` (Wilms, Allen & McCray 2000) accounts for the galactic absorption and two `diskbb` models (Makishima et al. 1986) correspond to the standard accretion disc components. We notice that the above model combinations is inadequate (e.g. $\chi^2_{\rm red} = 1.41$ for NGC 1313 X−1, ObsID-0693851201) in explaining the high energy tail of the spectra beyond ∼7 keV. Hence, a `simpl` (Steiner et al. 2009) model that delineates the fractional scattering of the seed photons into power-law distribution is included in the spectral fitting. Such a model combination (hereafter M1) `TBabs×(diskbb + simpl×diskbb)` is seen to describe the spectral shape of the BH-ULXs satisfactorily. For example, we obtain best spectral fit for NGC 1313 X−1 (ObsID-0693851201) with $\chi^2_{\rm red} = 1.19$ that resulted relatively hotter disc temperature ($kT_{\rm in}^{\rm hard}$) $= 2.08^{+0.46}_{-0.35}$ keV, softer disc temperature ($kT_{\rm in}^{\rm soft}$) $= 0.23^{+0.02}_{-0.02}$ keV, photon index ($\Gamma_{\rm simpl}$) $= 1.83^{+0.16}_{-0.09}$, seed photon scattered fraction ($f_{\rm scatt}$) $= 20.67^{+1.75}_{-0.92}$ per cent and column density ($N_{\rm H}$) $= 0.27^{+0.02}_{-0.02} \times 10^{22}$ atoms cm^{-2}. Accordingly, we employ model M1 to fit the spectra of four BH-ULXs and obtain statistically acceptable fit. However, we mention that for few observations, `simpl` model is not required mostly due to the lack of good quality data at high energies (see Table 3). The model fitted parameters and estimated parameters are presented in Table 3.

Next, we examine the spectral behaviour of the four BH-ULXs considering physically motivated model. While doing so, we begin with the model combination `TBabs×nthComp` to fit the spectra, where `nthComp` (Zdziarski, Johnson & Magdziarz 1996; Życki,

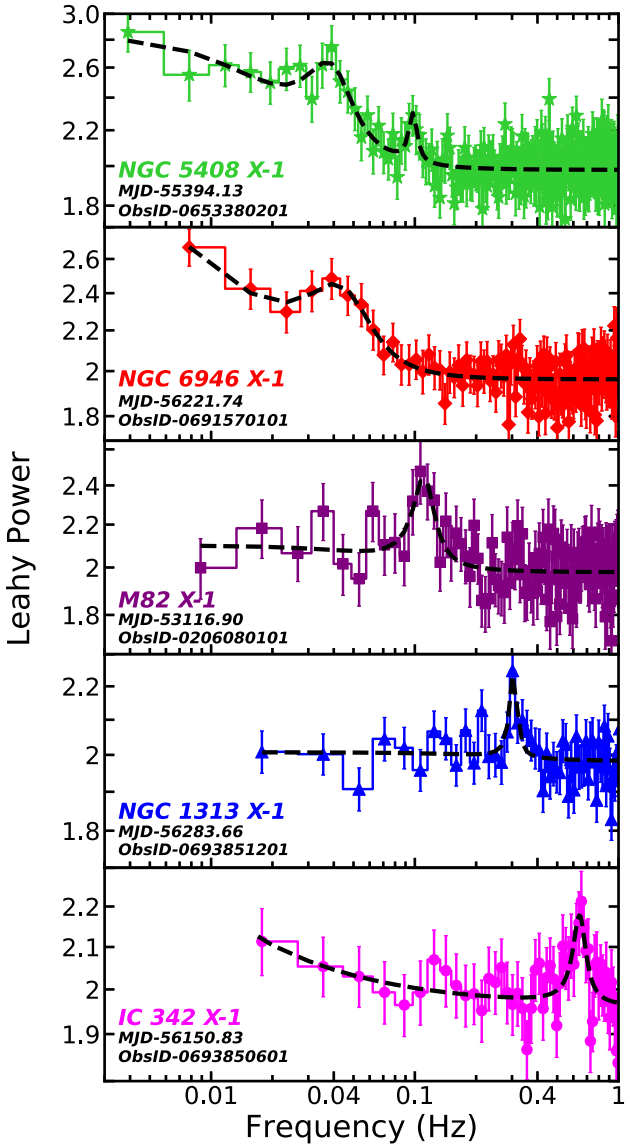

Figure 2. Leahy normalized PDS obtained from *EPIC-PN* data of the five BH-ULXs. In each panel, observed highest QPO frequency in 0.3–10 keV energy range for a given source is are presented along with source name and observation details. Each PDS is modelled with the combination of `Lorentzians` and a `constant`. See the text for details.

Done & Smith 1999) represents the thermally Comptonize continuum. The obtained fit yields poor $\chi^2_{\rm red} = 2.87$ ($\chi^2/dof = 1309/456$) for NGC 1313 X−1 (ObsID-0693851201) with noticeable residuals at lower energy. Hence, we include a `diskbb` model to fit the soft excess below ∼2 keV. Further, we tie the seed photon temperature of `nthComp` to the inner disc temperature of `diskbb` (Gladstone et al. 2009). Accordingly, the model combination `TBabs×(nthComp + diskbb)` (hereafter M2) provides a good fit ($\chi^2_{\rm red} = 1.20$ for NGC 1313 X−1; ObsID-0693851201). In Fig. 3, the variations of residuals (χ) in units of σ are presented in terms of energy in keV. In each panel of Fig. 3, we choose one particular observation for a given source and obtain the variation of χ from the spectral fitting of that observation using model M2. Note that the source names as well as the observation details are mentioned in each panel.

We further put efforts to fit the spectra with an alternative Comptonization model `compTT` (Titarchuk 1994; Hua & Titarchuk 1995) that results statistically acceptable fits, however, the electron temperature remains unconstrained in most of the observations. Moreover, we adopt the slim disc prescription (`diskpbb` in `XSPEC`; Mineshige et al. 1994; Hirano et al. 1995; Watarai et al. 2000; Kubota & Makishima 2004) for spectral fitting which yields worse fit with $\chi^2_{\rm red}$ exceeding 2 for all the sources. This evidently rules out the possibility of having slim accretion disc structure in these four BH-ULXs under consideration.

5.2 Spectral properties

In Fig. 4, we display the energy spectra fitted with model combination M2 corresponding to the observations that exhibits maximum QPO frequency (see Table 2) for four BH-ULXs. The source names and observation details are marked in the figure. The best-fitted model parameters and estimated parameters corresponding to the models M1 and M2 are tabulated in Tables 3 and 4, respectively. We find that the model M1 satisfactorily describes all the spectra in terms of two disc temperatures varying in the range of $0.16^{+0.01}_{-0.01} - 0.60^{+0.09}_{-0.05}$ and $0.75^{+0.03}_{-0.01} - 3.13^{+0.28}_{-0.21}$ keV, respectively. In addition, the photon index ($\Gamma_{\rm simpl}$) and the scattered fraction of seed photons ($f_{\rm scatt}$) in `simpl` component of the model M1 are obtained in the range of $1.09^{+0.15}_{-0.01} - 2.53^{+0.13}_{-0.12}$ and $1.99^{+1.07}_{-0.53} - 60.64^{+3.18}_{-2.55}$ per cent, respectively. The spectral fitting using model M2 constrains the electron temperature ($kT_{\rm e}$) and `nthComp` photon index ($\Gamma_{\rm nth}$) as $1.62^{+0.13}_{-0.12} - 3.76^{+1.15}_{-0.67}$ keV and $1.48^{+0.04}_{-0.11} - 2.65^{+0.19}_{-0.17}$, respectively. The inner disc temperature ($kT_{\rm in}$) is found to be in the range of $0.14^{+0.03}_{-0.02} - 0.54^{+0.15}_{-0.06}$ keV suggesting a cool accretion disc around the sources. Note that in few observations, we are unable to constrain the errors associated with the electron temperature and hence, it is kept fixed at its fitted values (see Table 4).

In order to understand the emission properties of BH-ULXs, we estimate the flux associated with each spectral component used in the model fitting. The flux is obtained by introducing the convolution model `cflux` (in `XSPEC`) after the absorption column density in the spectral fitting. While doing so, we freeze the normalizations of the spectral components at its best fitted values. With this, we compute the bolometric luminosity $L_{\rm bol} = F_{\rm bol} \times 4\pi d^2$, where $F_{\rm bol}$ is the bolometric flux in 0.1–100 keV energy range, and d is the source distance. In Tables 3 and 4, we present the computed $L_{\rm bol}$ for all the observations. We also compute the $L_{\rm disc}$ by calculating the bolometric disc flux $F_{\rm disc}$ in 0.1–100 keV range as $L_{\rm disc} = F_{\rm disc} \times 4\pi d^2$. Following Zdziarski et al. (1996) and Majumder et al. (2022), we calculate the optical depth (τ) and Compton y-parameter (y-par) for all the observations and obtain their ranges as $7 < \tau < 20$ and $1.16 \lesssim$ y-par $\lesssim 6.24$, respectively (see Table 4). These findings eventually indicate the existence of an optically thick and 'cool' corona surrounding the BH-ULXs under consideration.

5.3 Long-term spectral evolution

Here, we investigate the long-term evolution of the spectral parameters of each source under consideration. While doing so, we make use of physically motivated model M2 for spectral modelling. In Fig. 5, we show the variation of inner disc temperature ($kT_{\rm in}$), electron temperature ($kT_{\rm e}$), photon index ($\Gamma_{\rm nth}$), disc flux ($F_{\rm disc}$), Comptonized flux ($F_{\rm nth}$), Compton y-parameter (y-par), and bolometric luminosity ($L_{\rm bol}$) over the epochs of observation from top to bottom panel, respectively. We observe that all the sources except NGC 5408 X−1 show significant spectral evolution throughout the long-term monitoring for more than a decade. However, for NGC 5408 X−1, marginal variation in spectral properties is observed. We find that

Table 3. Details of the best fitted model parameters of combined *EPIC-PN* and *EPIC-MOS* spectra in 0.3–10 keV energy range with the model `TBabs×(diskbb + simpl×diskbb)` for four ULXs as mentioned in Table 1. In the table, $n_{\rm H}$ is the hydrogen column density, $kT_{\rm in}^{\rm soft}$ is the temperature of the soft disc component in keV, $kT_{\rm in}^{\rm hard}$ is the temperature of relatively hotter disc component in keV. $\Gamma_{\rm simpl}$ and $f_{\rm scatt}$ is the power index and Comptonized seed photon fraction of the `simpl` component, respectively. $\chi^2/d.o.f$ and $P_{\rm null}$ refer the reduced χ^2 and null hypothesis probability values. $F_{\rm disc}^{\rm soft}$ and $F_{\rm disc}^{\rm hard}$ are the flux values in erg cm^{-2} s^{-1} associated with hotter and softer `diskbb` component, respectively. $F_{\rm bol}$, and $L_{\rm bol}$ are the bolometric flux and luminosity, respectively. All the errors are computed with 90 per cent confidence level. See the text for details.

Source	ObsID	MJD	Model fitted parameters							Estimated parameters			
			$n_{\rm H}$	$kT_{\rm in}^{\rm soft}$	$kT_{\rm in}^{\rm hard}$	$\Gamma_{\rm simpl}$	$f_{\rm scatt}$	$\chi^2/d.o.f$	$P_{\rm null}^{\boxtimes}$	$F_{\rm disc}^{\rm soft}$	$F_{\rm disc}^{\rm hard}$	$F_{\rm bol}$	$L_{\rm bol}$
										(0.3–10 keV)		(0.1–100 keV)	
			(10^{22} cm^{-2})	(keV)	(keV)		(per cent)			(10^{-12} erg cm^{-2} s^{-1})			(10^{40} erg s^{-1})
NGC 1313 X-1	0106860101†	51834.14	$0.21^{+0.03}_{-0.03}$	$0.30^{+0.04}_{-0.03}$	$2.35^{+0.25}_{-0.21}$	–	–	131/131	0.47	$1.50^{+0.06}_{-0.06}$	$2.32^{+0.09}_{-0.09}$	$4.50^{+0.09}_{-0.09}$	0.97 ± 0.01
($d = 4.25$ Mpc[c])	0205230601†	53408.48	$0.40^{+0.02}_{-0.02}$	$0.19^{+0.01}_{-0.03}$	$0.76^{+0.03}_{-0.16}$	$1.09^{+0.15}_{-0.01}$	$60.30^{+1.86}_{-1.84}$	217/205	0.27	$5.01^{+0.19}_{-0.19}$	$3.32^{+0.13}_{-0.13}$	$12.69^{+0.32}_{-0.32}$	2.74 ± 0.07
	0405090101	54023.98	$0.30^{+0.02}_{-0.01}$	$0.21^{+0.01}_{-0.01}$	$2.07^{+0.22}_{-0.17}$	$1.76^{+0.08}_{-0.07}$	$14.20^{+1.29}_{-1.25}$	502/445	0.03	$2.36^{+0.02}_{-0.02}$	$0.92^{+0.01}_{-0.01}$	$6.63^{+0.04}_{-0.04}$	1.43 ± 0.01
	0693850501	56277.67	$0.27^{+0.03}_{-0.02}$	$0.24^{+0.02}_{-0.04}$	$2.38^{+0.71}_{-0.44}$	$1.85^{+0.15}_{-0.14}$	$19.70^{+1.23}_{-1.82}$	489/439	0.05	$2.53^{+0.03}_{-0.03}$	$1.00^{+0.03}_{-0.03}$	$7.03^{+0.08}_{-0.08}$	1.52 ± 0.02
	0693851201	56283.66	$0.27^{+0.02}_{-0.02}$	$0.23^{+0.02}_{-0.02}$	$2.08^{+0.46}_{-0.35}$	$1.83^{+0.16}_{-0.09}$	$20.67^{+1.75}_{-0.92}$	518/454	0.03	$2.57^{+0.03}_{-0.03}$	$0.82^{+0.04}_{-0.04}$	$7.20^{+0.05}_{-0.05}$	1.56 ± 0.01
	0742590301†	56843.97	$0.29^{+0.01}_{-0.01}$	$0.24^{+0.01}_{-0.01}$	$0.75^{+0.03}_{-0.01}$	$2.53^{+0.02}_{-0.02}$	$60.64^{+3.18}_{-2.55}$	572/433	0.01	$3.41^{+0.05}_{-0.05}$	$3.59^{+0.03}_{-0.03}$	$11.09^{+0.05}_{-0.05}$	2.40 ± 0.01
	0742490101†	57111.19	$0.27^{+0.01}_{-0.01}$	$0.25^{+0.02}_{-0.03}$	$1.09^{+0.06}_{-0.05}$	$1.38^{+0.13}_{-0.11}$	$53.63^{+4.89}_{-2.82}$	360/266	0.01	$1.81^{+0.03}_{-0.03}$	$1.92^{+0.03}_{-0.03}$	$5.91^{+0.05}_{-0.05}$	1.28 ± 0.01
	0803990101†	57918.89	$0.29^{+0.01}_{-0.01}$	$0.26^{+0.01}_{-0.01}$	$1.07^{+0.03}_{-0.02}$	$1.18^{+0.06}_{-0.05}$	$33.82^{+3.80}_{-2.54}$	682/486	0.01	$3.35^{+0.02}_{-0.02}$	$4.95^{+0.03}_{-0.03}$	$10.87^{+0.05}_{-0.05}$	2.35 ± 0.01
	0803990301†	57996.68	$0.29^{+0.01}_{-0.02}$	$0.23^{+0.01}_{-0.01}$	$1.30^{+0.09}_{-0.02}$	$1.35^{+0.08}_{-0.07}$	$44.47^{+4.33}_{-3.12}$	478/422	0.03	$2.46^{+0.04}_{-0.04}$	$2.48^{+0.04}_{-0.04}$	$7.18^{+0.09}_{-0.08}$	1.55 ± 0.02
	0803990601†	58096.46	$0.27^{+0.01}_{-0.01}$	$0.29^{+0.01}_{-0.01}$	$1.09^{+0.01}_{-0.03}$	$1.09^{+0.05}_{-0.02}$	$34.52^{+0.73}_{-0.70}$	614/455	0.01	$3.14^{+0.04}_{-0.04}$	$5.39^{+0.06}_{-0.06}$	$9.86^{+0.08}_{-0.08}$	2.13 ± 0.02
NGC 5408 X-1	0112290501†	52121.54	0.11*	$0.18^{+0.01}_{-0.01}$	$0.82^{+0.09}_{-0.08}$	–	–	128/130	0.53	$3.24^{+0.13}_{-0.13}$	$0.86^{+0.05}_{-0.05}$	$5.28^{+0.24}_{-0.24}$	1.46 ± 0.06
($d = 4.8$ Mpc[e])	0112291001†	52484.35	$0.12^{+0.04}_{-0.03}$	$0.19^{+0.02}_{-0.02}$	$0.88^{+0.42}_{-0.19}$	–	–	125/136	0.74	$2.12^{+0.02}_{-0.02}$	$0.89^{+0.06}_{-0.06}$	$4.27^{+0.12}_{-0.12}$	1.18 ± 0.03
	0112291201†	52667.01	$0.13^{+0.06}_{-0.05}$	$0.19^{+0.03}_{-0.03}$	$1.08^{+0.22}_{-0.15}$	–	–	92/97	0.62	$2.01^{+0.11}_{-0.11}$	$0.77^{+0.05}_{-0.05}$	$3.11^{+0.15}_{-0.15}$	0.86 ± 0.04
	0302900101	53748.77	$0.11^{+0.01}_{-0.01}$	$0.16^{+0.01}_{-0.01}$	$0.76^{+0.06}_{-0.04}$	$2.35^{+0.14}_{-0.16}$	$7.93^{+2.51}_{-2.27}$	423/337	0.01	$2.21^{+0.02}_{-0.02}$	$0.39^{+0.01}_{-0.01}$	$4.99^{+0.03}_{-0.03}$	1.38 ± 0.01
	0500750101	54478.79	$0.11^{+0.01}_{-0.01}$	$0.17^{+0.01}_{-0.01}$	$0.77^{+0.06}_{-0.04}$	$2.14^{+0.25}_{-0.29}$	$6.61^{+4.10}_{-2.96}$	320/294	0.14	$1.84^{+0.03}_{-0.03}$	$0.49^{+0.02}_{-0.02}$	$4.29^{+0.05}_{-0.05}$	1.18 ± 0.01
	0653380201	55394.13	$0.11^{+0.01}_{-0.01}$	$0.17^{+0.01}_{-0.01}$	$0.89^{+0.13}_{-0.09}$	$2.46^{+0.15}_{-0.17}$	$14.08^{+3.63}_{-3.84}$	321/301	0.21	$2.26^{+0.02}_{-0.02}$	$0.39^{+0.02}_{-0.02}$	$5.34^{+0.04}_{-0.04}$	1.47 ± 0.01
	0653380301	55396.13	$0.09^{+0.01}_{-0.01}$	$0.18^{+0.01}_{-0.01}$	$0.99^{+0.18}_{-0.12}$	$2.53^{+0.13}_{-0.12}$	$19.75^{+3.79}_{-3.61}$	429/364	0.01	$1.87^{+0.01}_{-0.01}$	$0.31^{+0.01}_{-0.01}$	$4.48^{+0.03}_{-0.03}$	1.24 ± 0.01
	0653380401	55587.67	$0.10^{+0.01}_{-0.01}$	$0.18^{+0.01}_{-0.01}$	$0.81^{+0.06}_{-0.04}$	$2.23^{+0.19}_{-0.16}$	$8.73^{+3.96}_{-2.50}$	398/356	0.06	$1.97^{+0.02}_{-0.02}$	$0.51^{+0.01}_{-0.01}$	$4.49^{+0.03}_{-0.03}$	1.24 ± 0.01
	0653380501	55589.65	$0.12^{+0.01}_{-0.01}$	$0.18^{+0.01}_{-0.01}$	$0.81^{+0.03}_{-0.03}$	$1.30^{+0.24}_{-0.14}$	$16.40^{+3.02}_{-1.20}$	402/341	0.01	$1.90^{+0.03}_{-0.03}$	$0.94^{+0.02}_{-0.02}$	$4.24^{+0.04}_{-0.04}$	1.17 ± 0.01
	0723130301	56699.02	$0.11^{+0.01}_{-0.01}$	$0.16^{+0.01}_{-0.01}$	$0.81^{+0.05}_{-0.04}$	$1.45^{+0.11}_{-0.09}$	$1.99^{+1.07}_{-0.53}$	280/244	0.06	$1.91^{+0.04}_{-0.04}$	$0.71^{+0.02}_{-0.02}$	$4.20^{+0.06}_{-0.06}$	1.16 ± 0.02
	0723130401	56701.02	$0.11^{+0.02}_{-0.01}$	$0.18^{+0.01}_{-0.02}$	$0.93^{+0.12}_{-0.09}$	$2.34^{+0.25}_{-0.25}$	$11.09^{+5.08}_{-4.33}$	268/262	0.38	$1.91^{+0.03}_{-0.03}$	$0.44^{+0.02}_{-0.02}$	$4.44^{+0.05}_{-0.05}$	1.22 ± 0.01
NGC 6946 X-1	0500730201	54406.91	$0.31^{+0.04}_{-0.04}$	$0.17^{+0.02}_{-0.01}$	$1.13^{+0.11}_{-0.10}$	$2.40^{+0.24}_{-0.22}$	$16.49^{+3.52}_{-2.45}$	93/104	0.77	$1.32^{+0.04}_{-0.04}$	$0.15^{+0.02}_{-0.02}$	$3.08^{+0.07}_{-0.07}$	2.20 ± 0.05
($d = 7.72$ Mpc[b])	0500730101	54412.94	$0.27^{+0.03}_{-0.03}$	$0.20^{+0.01}_{-0.01}$	$0.84^{+0.13}_{-0.13}$	$1.50^{+0.35}_{-0.23}$	$4.64^{+2.00}_{-0.93}$	195/181	0.21	$1.19^{+0.06}_{-0.06}$	$0.31^{+0.03}_{-0.03}$	$2.66^{+0.07}_{-0.06}$	1.90 ± 0.04
	0691570101	56221.74	$0.31^{+0.03}_{-0.02}$	$0.18^{+0.01}_{-0.01}$	$1.12^{+0.40}_{-0.23}$	$2.41^{+0.24}_{-0.20}$	$14.07^{+4.02}_{-3.77}$	325/330	0.56	$1.83^{+0.03}_{-0.03}$	$0.18^{+0.02}_{-0.02}$	$4.07^{+0.05}_{-0.05}$	2.90 ± 0.04
	0870830101	59038.93	$0.32^{+0.06}_{-0.06}$	$0.21^{+0.03}_{-0.02}$	$1.30^{+0.17}_{-0.14}$	–	–	142/135	0.32	$1.89^{+0.08}_{-0.08}$	$0.67^{+0.05}_{-0.04}$	$3.48^{+0.15}_{-0.16}$	2.48 ± 0.11
	0870830201	59198.32	$0.37^{+0.08}_{-0.08}$	$0.18^{+0.03}_{-0.02}$	$1.07^{+0.14}_{-0.11}$	–	–	87/82	0.31	$2.85^{+0.20}_{-0.19}$	$0.69^{+0.05}_{-0.05}$	$5.34^{+0.37}_{-0.37}$	3.81 ± 0.26
	0870830301	59308.22	$0.28^{+0.05}_{-0.05}$	$0.22^{+0.03}_{-0.02}$	$1.30^{+0.14}_{-0.12}$	–	–	122/134	0.75	$1.44^{+0.07}_{-0.06}$	$0.62^{+0.03}_{-0.03}$	$2.74^{+0.06}_{-0.06}$	1.95 ± 0.04
	0870830401	59359.89	$0.32^{+0.07}_{-0.06}$	$0.19^{+0.03}_{-0.02}$	$1.22^{+0.14}_{-0.12}$	–	–	88/100	0.78	$1.62^{+0.07}_{-0.07}$	$0.56^{+0.03}_{-0.03}$	$3.07^{+0.08}_{-0.07}$	2.19 ± 0.06
IC 342 X-1	0093640901†	51951.06	$0.58^{+0.08}_{-0.06}$	$0.42^{+0.08}_{-0.06}$	$2.78^{+0.38}_{-0.27}$	–	–	136/138	0.52	$0.91^{+0.08}_{-0.08}$	$2.41^{+0.11}_{-0.11}$	$3.91^{+0.18}_{-0.18}$	0.61 ± 0.03
($d = 3.61$ Mpc[d])	0206890101†	53055.31	$0.63^{+0.03}_{-0.03}$	$0.54^{+0.06}_{-0.06}$	$2.13^{+0.13}_{-0.11}$	–	–	284/304	0.79	$2.35^{+0.11}_{-0.11}$	$5.83^{+0.13}_{-0.13}$	$9.02^{+0.23}_{-0.22}$	1.41 ± 0.03
	0206890201†	53234.82	$0.65^{+0.04}_{-0.03}$	$0.43^{+0.03}_{-0.03}$	$2.68^{+0.17}_{-0.15}$	–	–	290/276	0.26	$1.49^{+0.03}_{-0.03}$	$2.57^{+0.05}_{-0.05}$	$4.72^{+0.05}_{-0.05}$	0.74 ± 0.01
	0693850601	56150.83	$0.74^{+0.04}_{-0.04}$	$0.29^{+0.02}_{-0.02}$	$1.74^{+0.18}_{-0.16}$	$1.30^{+0.12}_{-0.13}$	$13.43^{+2.93}_{-2.47}$	330/360	0.86	$2.09^{+0.07}_{-0.07}$	$1.48^{+0.07}_{-0.07}$	$5.96^{+0.08}_{-0.08}$	0.93 ± 0.01
	0693851301†	56156.84	$0.59^{+0.02}_{-0.02}$	$0.48^{+0.03}_{-0.02}$	$2.44^{+0.09}_{-0.08}$	–	–	402/377	0.17	$1.46^{+0.04}_{-0.04}$	$3.05^{+0.06}_{-0.06}$	$5.13^{+0.06}_{-0.06}$	0.80 ± 0.01

Notes. †Non-detection of QPO.
*Frozen parameter value.
$^{\boxtimes}P_{\rm null} < 0.1$ yielded due to excess residuals at 0.56 and 1 keV in some of the observations of NGC 1313 X−1 and NGC 5408 X−1.
[e] Luangtip et al. (2021), [c] Tully et al. (2016), [b] Anand et al. (2018), [d] Middleton et al. (2015).

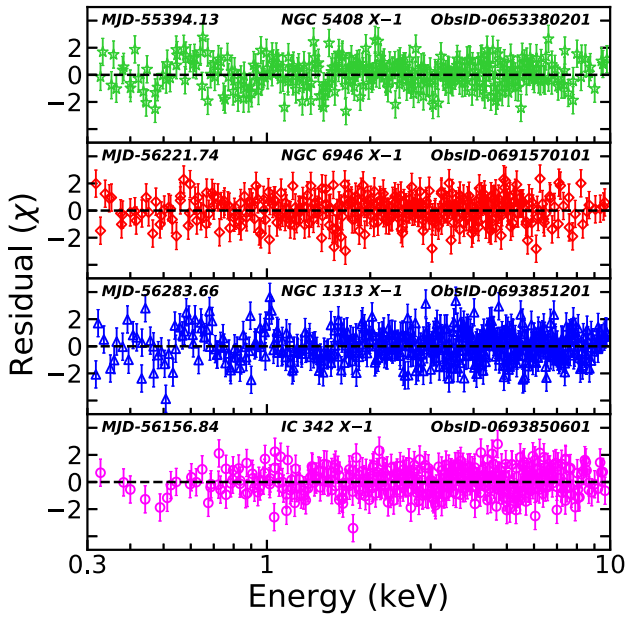

Figure 3. Variation of the residuals in units of σ. In each panel, the residuals obtained from the model fitting of combined *EPIC-PN* and *EPIC-MOS* energy spectra with the model `TBabs×(diskbb + nthComp)` are shown. See the text for details.

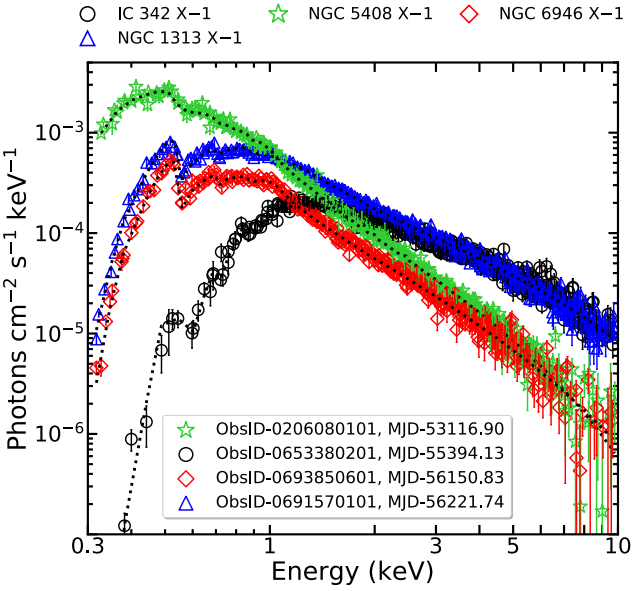

Figure 4. Combined *EPIC-PN* and *EPIC-MOS* energy spectra (0.3–10 keV) of four BH-ULXs under consideration. Each spectrum is fitted with the model `TBabs×(diskbb + nthComp)`. The observation details are mentioned in the inset. See the text for details.

NGC 1313 X−1 and IC 342 X−1 are dominated by the Comptonized flux ($F_{\rm nth} \sim 3$–45×10^{-12} erg cm^{-2} s^{-1}) whereas NGC 6946 X−1 and NGC 5408 X−1 are seen to be disc dominated ($F_{\rm disc} \sim 1$–5×10^{-12} erg cm^{-2} s^{-1}). In addition, for NGC 5408 X−1 and NGC 6946 X−1, the photon index is found to be more steeper ($\Gamma_{\rm nth} \gtrsim 2$) in comparison to other sources ($\Gamma_{\rm nth} \lesssim 2$), which further confirms the softer nature of these two sources. We calculate the y-parameter and find that the amount of Comptonization is high (y-par ∼2–6) for NGC 1313 X−1 and IC 342 X−1 as compared to the remaining two sources. The electron temperature manifests an overall variation in the range of ∼2–4 keV for all the sources. Interestingly, we find that the disc temperature demonstrates a minimal variation in all the sources except IC 342 X−1, which possibly harbour variable disc of higher temperatures. Further, we observe that NGC 6946 X−1 is the most luminous ULX in our sample, showing maximum long-term variation in the luminosity as well.

6 CORRELATIONS AMONG SPECTROTEMPORAL OBSERVABLES

In this section, we examine the correlations among the various observables obtained from both timing and spectral analyses of the four BH-ULXs. With this, we put efforts to understand the spectrotemporal properties of these sources.

6.1 Correlation in $L_{\rm disc} - T_{\rm col}$ plane

We carry out the correlation study of bolometric disc luminosity ($L_{\rm disc}$) and colour corrected inner disc temperature ($T_{\rm col}$). Following Done & Davis (2008), we compute $T_{\rm col} = f \times T_{\rm in}$ for spectral fitting with model M2 (see Table 4), where f (= 1.7) refers to the spectral hardening factor. The obtained results are presented in Fig. 6, where $L_{\rm disc}$ is plotted as function of $T_{\rm col}$. We calculate the Pearson correlation coefficient (ρ) to deduce the correlation between $L_{\rm disc}$ and $T_{\rm col}$ and observe an anticorrelation relation with $\rho \sim -0.81$ for NGC 1313 X−1 and IC 342 X−1, and $\rho \sim -0.89$ for NGC 6946 X−1. However, a weak negative correlation with $\rho \sim -0.27$ is observed for NGC 5408 *X*–1. Further, we run an MCMC simulation using the Goodman–Weare algorithm (Goodman & Weare 2010) with a chain length of 20 000 and check for possible correlation (see Appendix B) between disc flux ($F_{\rm disc}$) and inner disc temperature ($T_{\rm in}$). We find that $F_{\rm disc}$ depends on $T_{\rm in}$ for each source that rules out degeneracy and possibly causes the observed correlation in $L_{\rm disc} - T_{\rm col}$ plane. Note that the above correlations are suitably described with an empirical power-law $L_{\rm disc} \propto T_{\rm col}^{\alpha}$ (Rybicki & Lightman 1979), where α denotes the power-law index. A combined fitting for NGC 1313 X−1 and IC 342 X−1 yields $\alpha = -3.58 \pm 0.04$, whereas a more steeper index $\alpha = -8.93 \pm 0.11$ is obtained for NGC 6946 X−1. However, the fitting of the distribution in temperature–luminosity plane of NGC 5408 X-1 results $\alpha = -10.31 \pm 0.10$. The best-fitting power-law distributions are shown in upper panel of Fig. 6 along with the residuals in the lower panel.

6.2 Correlation in $L_{\rm bol} - \Gamma_{\rm nth}$ plane

We investigate the correlation between $L_{\rm bol}$ and the `nthComp` photon index ($\Gamma_{\rm nth}$) for four BH-ULXs. The obtained results are depicted in Fig. 7, where the variation of $L_{\rm bol}$ with $\Gamma_{\rm nth}$ is presented for each of the sources. Here, we observe strong positive correlation between $L_{\rm bol}$ and $\Gamma_{\rm nth}$ with Pearson correlation coefficient +0.81, +0.92, +0.94, and +0.92 for IC 342 X−1, NGC 1313 X−1, NGC 5408 X−1, and NGC 6946 X−1, respectively. Such a correlation is quantified using linear relation as $L_{\rm bol} = A\Gamma_{\rm nth} + C$, where A and C are source specific arbitrary constants. In the figure, the fitted functional relations are shown using dot-dashed curves in magenta, green, red, and blue for four BH-ULXs. Indeed, for NGC 6946 X−1, three data points at lower luminosities are excluded during fitting as they appear to be outliers. Note that the best-fitted points with higher luminosity belong

Table 4. Best-fitted spectral parameters obtained with the model `TBabs×(diskbb + nthComp)` for four ULXs in the sample. In the table, n_H is the hydrogen column density, kT_e is the electron temperature in keV, Γ_{nth} is the `nthComp` photon index, τ is the optical depth, and kT_{in} is the inner disc temperature in keV. $\chi^2/d.o.f$ and P_{null} refer the reduced χ^2 and null hypothesis probability values. F_{disc} and F_{nth} are the flux values in units of erg cm^{-2} s^{-1} associated with `diskbb` and `nthComp` components, respectively. F_{bol}, L_{bol}, and L_{disc} are the bolometric flux, total luminosity, and disc luminosity, respectively. All the errors are computed with 90 per cent confidence level. See the text for details.

			Model fitted parameters						Estimated parameters							
Source	ObsID	MJD	n_H	kT_e	Γ_{nth}	kT_{in}	$\chi^2/d.o.f$	P_{null} ⊠	F_{disc} (0.3–10 keV)	F_{nth}	F_{bol} (0.1–100 keV)	F_{disc}	L_{bol}	L_{disc}	τ	y-par
(Distance)			(10^{22} cm^{-2})	(keV)		(keV)			(10^{-12} erg cm^{-2} s^{-1})				(10^{40} erg s^{-1})			
NGC 1313 X-1	0106860101†	51834.14	$0.25^{+0.03}_{-0.04}$	$2.22^{+0.51}_{-0.31}$	$1.66^{+0.07}_{-0.09}$	$0.24^{+0.04}_{-0.03}$	128/130	0.52	$1.44^{+0.08}_{-0.08}$	$2.87^{+0.09}_{-0.09}$	$5.32^{+0.11}_{-0.10}$	$2.00^{+0.11}_{-0.11}$	1.15 ± 0.02	0.43 ± 0.02	15.49 ± 2.36	4.16 ± 0.57
($d = 4.25$ Mpc)	0205230601†	53408.48	$0.36^{+0.08}_{-0.07}$	2*	$1.74^{+0.08}_{-0.04}$	$0.19^{+0.04}_{-0.03}$	232/207	0.11	$3.44^{+0.16}_{-0.16}$	$3.43^{+0.11}_{-0.11}$	$9.31^{+0.24}_{-0.24}$	$5.44^{+0.25}_{-0.25}$	2.01 ± 0.05	1.18 ± 0.05	15.22 ± 1.07	3.62 ± 0.51
	0 405 090 101	54023.98	$0.31^{+0.01}_{-0.01}$	$2.31^{+0.14}_{-0.12}$	$1.71^{+0.03}_{-0.03}$	$0.19^{+0.01}_{-0.01}$	532/446	0.02	$2.07^{+0.02}_{-0.02}$	$3.22^{+0.02}_{-0.01}$	$6.90^{+0.05}_{-0.05}$	$3.21^{+0.05}_{-0.05}$	1.49 ± 0.01	0.69 ± 0.01	14.46 ± 0.62	3.77 ± 0.21
	0 693 850 501	56277.67	$0.28^{+0.02}_{-0.02}$	$2.53^{+0.22}_{-0.17}$	$1.73^{+0.04}_{-0.04}$	$0.23^{+0.02}_{-0.01}$	479/440	0.10	$1.93^{+0.04}_{-0.04}$	$3.60^{+0.05}_{-0.05}$	$6.95^{+0.07}_{-0.07}$	$2.77^{+0.05}_{-0.05}$	1.50 ± 0.02	0.59 ± 0.01	13.51 ± 0.81	3.61 ± 0.26
	0 693 851 201	56283.66	$0.28^{+0.02}_{-0.02}$	$2.72^{+0.25}_{-0.19}$	$1.78^{+0.03}_{-0.03}$	$0.22^{+0.01}_{-0.01}$	547/455	0.01	$1.98^{+0.03}_{-0.03}$	$3.80^{+0.04}_{-0.04}$	$7.35^{+0.05}_{-0.05}$	$2.90^{+0.05}_{-0.05}$	1.59 ± 0.01	0.63 ± 0.01	12.42 ± 0.71	3.28 ± 0.17
	0742590301†	56843.97	$0.33^{+0.03}_{-0.03}$	$2.16^{+0.21}_{-0.16}$	$2.10^{+0.04}_{-0.04}$	$0.19^{+0.02}_{-0.01}$	592/434	0.01	$2.34^{+0.06}_{-0.06}$	$7.87^{+0.05}_{-0.05}$	$12.86^{+0.06}_{-0.06}$	$3.69^{+0.10}_{-0.10}$	2.78 ± 0.01	0.80 ± 0.02	11.14 ± 0.67	2.10 ± 0.11
	0742490101†	57111.19	$0.29^{+0.03}_{-0.02}$	$2.86^{+1.25}_{-0.50}$	$1.74^{+0.04}_{-0.05}$	$0.21^{+0.02}_{-0.02}$	355/267	0.03	$1.69^{+0.04}_{-0.04}$	$3.05^{+0.04}_{-0.04}$	$6.16^{+0.06}_{-0.06}$	$2.51^{+0.06}_{-0.06}$	1.33 ± 0.01	0.54 ± 0.01	12.51 ± 3.06	3.49 ± 0.26
	0803990101†	57918.89	$0.34^{+0.01}_{-0.01}$	$2.69^{+0.16}_{-0.14}$	$2.04^{+0.02}_{-0.02}$	$0.20^{+0.01}_{-0.01}$	684/540	0.01	$2.69^{+0.04}_{-0.04}$	$7.31^{+0.03}_{-0.03}$	$12.74^{+0.05}_{-0.05}$	$4.16^{+0.07}_{-0.07}$	2.75 ± 0.01	0.90 ± 0.02	10.25 ± 0.37	2.21 ± 0.06
	0803990301†	57996.68	$0.33^{+0.02}_{-0.02}$	$2.25^{+0.16}_{-0.13}$	$1.70^{+0.02}_{-0.02}$	$0.20^{+0.01}_{-0.01}$	471/420	0.05	$2.62^{+0.05}_{-0.05}$	$3.43^{+0.01}_{-0.01}$	$7.99^{+0.09}_{-0.09}$	$4.07^{+0.07}_{-0.07}$	1.72 ± 0.02	0.88 ± 0.02	14.80 ± 0.64	3.85 ± 0.15
	0803990601†	58096.46	$0.32^{+0.02}_{-0.01}$	$2.14^{+0.13}_{-0.11}$	$2.08^{+0.02}_{-0.02}$	$0.20^{+0.01}_{-0.01}$	642/456	0.01	$1.99^{+0.05}_{-0.05}$	$7.13^{+0.07}_{-0.07}$	$11.16^{+0.09}_{-0.09}$	$2.97^{+0.08}_{-0.08}$	2.41 ± 0.02	0.64 ± 0.02	11.35 ± 0.41	2.15 ± 0.06
NGC 5408 X-1	0112290501†	52121.54	0.11*	2.01*	$2.65^{+0.19}_{-0.17}$	$0.16^{+0.01}_{-0.01}$	125/129	0.57	$2.73^{+0.12}_{-0.12}$	$1.82^{+0.09}_{-0.09}$	$7.11^{+0.20}_{-0.20}$	$4.78^{+0.21}_{-0.21}$	1.96 ± 0.06	1.32 ± 0.06	8.62 ± 0.77	1.16 ± 0.21
($d = 4.8$ Mpc)	0112291001†	52484.35	$0.12^{+0.04}_{-0.03}$	1.97*	$2.13^{+0.43}_{-0.45}$	$0.18^{+0.03}_{-0.03}$	126/136	0.71	$1.85^{+0.09}_{-0.09}$	$1.47^{+0.07}_{-0.07}$	$4.72^{+0.13}_{-0.13}$	$3.01^{+0.14}_{-0.14}$	1.30 ± 0.04	0.83 ± 0.04	11.51 ± 3.26	2.04 ± 1.10
	0112291201†	52667.01	$0.13^{+0.06}_{-0.05}$	2.01*	$2.19^{+0.21}_{-0.21}$	$0.18^{+0.03}_{-0.03}$	92/96	0.58	$1.89^{+0.11}_{-0.11}$	$1.30^{+0.09}_{-0.09}$	$4.64^{+0.16}_{-0.16}$	$3.10^{+0.17}_{-0.17}$	1.28 ± 0.04	0.85 ± 0.05	10.97 ± 1.39	1.89 ± 0.48
	0 302 900 101	53748.77	$0.12^{+0.01}_{-0.01}$	$1.62^{+0.16}_{-0.14}$	$2.31^{+0.07}_{-0.01}$	$0.16^{+0.01}_{-0.01}$	438/338	0.01	$1.87^{+0.01}_{-0.01}$	$1.45^{+0.01}_{-0.01}$	$5.27^{+0.02}_{-0.02}$	$3.36^{+0.04}_{-0.04}$	1.45 ± 0.01	0.93 ± 0.01	11.54 ± 0.78	1.69 ± 0.13
	0 500 750 101	54478.79	$0.12^{+0.01}_{-0.01}$	$1.62^{+0.18}_{-0.14}$	$2.24^{+0.08}_{-0.02}$	$0.16^{+0.01}_{-0.01}$	333/295	0.07	$1.50^{+0.03}_{-0.03}$	$1.42^{+0.03}_{-0.03}$	$4.49^{+0.05}_{-0.05}$	$2.65^{+0.04}_{-0.04}$	1.24 ± 0.01	0.73 ± 0.01	12.01 ± 0.93	1.83 ± 0.17
	0 653 380 201	55394.13	$0.11^{+0.01}_{-0.01}$	$1.69^{+0.19}_{-0.14}$	$2.27^{+0.07}_{-0.05}$	$0.16^{+0.01}_{-0.01}$	334/303	0.11	$1.72^{+0.02}_{-0.02}$	$1.90^{+0.02}_{-0.02}$	$5.40^{+0.04}_{-0.04}$	$2.98^{+0.07}_{-0.07}$	1.49 ± 0.01	0.82 ± 0.02	11.53 ± 0.86	1.76 ± 0.14
	0 653 380 301	55396.13	$0.10^{+0.01}_{-0.01}$	$1.84^{+0.20}_{-0.15}$	$2.27^{+0.07}_{-0.07}$	$0.17^{+0.01}_{-0.01}$	419/366	0.03	$1.41^{+0.02}_{-0.02}$	$1.79^{+0.02}_{-0.02}$	$4.57^{+0.03}_{-0.03}$	$2.34^{+0.05}_{-0.05}$	1.26 ± 0.01	0.65 ± 0.01	11.00 ± 0.80	1.74 ± 0.14
	0 653 380 401	55587.67	$0.11^{+0.01}_{-0.01}$	$1.62^{+0.13}_{-0.12}$	$2.24^{+0.01}_{-0.01}$	$0.17^{+0.01}_{-0.01}$	404/358	0.05	$1.58^{+0.02}_{-0.02}$	$1.64^{+0.02}_{-0.02}$	$4.75^{+0.03}_{-0.03}$	$2.68^{+0.06}_{-0.06}$	1.31 ± 0.02	0.74 ± 0.02	12.01 ± 0.54	1.83 ± 0.03
	0 653 380 501	55589.65	$0.11^{+0.01}_{-0.01}$	$1.62^{+0.17}_{-0.15}$	$2.21^{+0.08}_{-0.01}$	$0.17^{+0.01}_{-0.01}$	415/342	0.01	$1.53^{+0.02}_{-0.02}$	$1.56^{+0.02}_{-0.02}$	$4.50^{+0.04}_{-0.04}$	$2.56^{+0.03}_{-0.03}$	1.24 ± 0.01	0.71 ± 0.01	12.22 ± 0.92	1.89 ± 0.18
	0 723 130 301	56699.02	$0.12^{+0.01}_{-0.01}$	$1.62^{+0.24}_{-0.19}$	$2.18^{+0.13}_{-0.02}$	$0.17^{+0.01}_{-0.01}$	297/244	0.02	$1.54^{+0.04}_{-0.04}$	$1.45^{+0.04}_{-0.04}$	$4.36^{+0.06}_{-0.06}$	$2.59^{+0.05}_{-0.05}$	1.20 ± 0.02	0.71 ± 0.01	12.44 ± 1.41	1.96 ± 0.31
	0 723 130 401	56701.02	$0.11^{+0.01}_{-0.01}$	$1.62^{+0.18}_{-0.16}$	$2.17^{+0.02}_{-0.02}$	$0.17^{+0.01}_{-0.01}$	272/263	0.34	$1.58^{+0.03}_{-0.03}$	$1.55^{+0.03}_{-0.03}$	$4.62^{+0.04}_{-0.04}$	$2.67^{+0.05}_{-0.05}$	1.27 ± 0.01	0.74 ± 0.01	12.52 ± 0.78	1.98 ± 0.05
NGC 6946 X-1	0 500 730 201	54406.91	$0.28^{+0.11}_{-0.10}$	2.19*	$2.18^{+0.06}_{-0.07}$	$0.18^{+0.04}_{-0.02}$	179/203	0.88	$0.82^{+0.04}_{-0.04}$	$0.93^{+0.04}_{-0.04}$	$2.42^{+0.06}_{-0.06}$	$1.29^{+0.06}_{-0.06}$	1.73 ± 0.04	0.93 ± 0.04	10.52 ± 0.45	1.89 ± 0.16
($d = 7.72$ Mpc)	0 500 730 101	54412.94	$0.28^{+0.07}_{-0.05}$	3.20*	$2.11^{+0.11}_{-0.06}$	$0.18^{+0.03}_{-0.03}$	163/180	0.81	$1.04^{+0.05}_{-0.05}$	$0.96^{+0.04}_{-0.04}$	$2.87^{+0.07}_{-0.07}$	$1.69^{+0.08}_{-0.08}$	2.05 ± 0.05	1.21 ± 0.06	8.87 ± 0.64	1.97 ± 0.28
	0 691 570 101	56221.74	$0.32^{+0.04}_{-0.05}$	$2.23^{+0.07}_{-0.07}$	$2.25^{+0.14}_{-0.15}$	$0.16^{+0.01}_{-0.01}$	326/331	0.57	$1.64^{+0.04}_{-0.04}$	$1.31^{+0.03}_{-0.03}$	$4.38^{+0.10}_{-0.10}$	$2.77^{+0.06}_{-0.06}$	3.12 ± 0.07	1.98 ± 0.04	9.98 ± 0.84	1.74 ± 0.30
	0 870 830 101	59038.93	$0.43^{+0.10}_{-0.09}$	2.69*	$2.22^{+0.15}_{-0.14}$	$0.16^{+0.03}_{-0.02}$	135/135	0.48	$3.61^{+0.17}_{-0.16}$	$1.25^{+0.09}_{-0.08}$	$7.96^{+0.36}_{-0.36}$	$6.47^{+0.31}_{-0.29}$	5.68 ± 0.26	4.61 ± 0.22	9.14 ± 0.83	1.75 ± 0.32
	0 870 830 201	59198.32	$0.47^{+0.12}_{-0.11}$	1.72*	$2.23^{+0.18}_{-0.16}$	$0.14^{+0.03}_{-0.02}$	84/82	0.42	$5.17^{+0.36}_{-0.36}$	$1.28^{+0.09}_{-0.09}$	$11.23^{+0.82}_{-0.81}$	$10.17^{+0.74}_{-0.71}$	8.01 ± 0.58	7.25 ± 0.51	12.37 ± 1.18	1.94 ± 0.22
	0 870 830 301	59308.22	$0.34^{+0.08}_{-0.07}$	1.62*	$2.03^{+0.12}_{-0.12}$	$0.17^{+0.03}_{-0.02}$	119/134	0.81	$1.92^{+0.08}_{-0.08}$	$0.97^{+0.05}_{-0.04}$	$4.27^{+0.10}_{-0.09}$	$3.16^{+0.15}_{-0.14}$	3.05 ± 0.07	2.25 ± 0.08	13.69 ± 1.10	2.37 ± 0.38
	0 870 830 401	59359.89	$0.37^{+0.10}_{-0.08}$	1.62*	$2.06^{+0.13}_{-0.12}$	$0.16^{+0.03}_{-0.02}$	85/100	0.85	$2.37^{+0.11}_{-0.10}$	$0.91^{+0.04}_{-0.04}$	$5.23^{+0.12}_{-0.12}$	$4.18^{+0.20}_{-0.19}$	3.73 ± 0.09	2.98 ± 0.14	13.42 ± 1.14	2.28 ± 0.39
IC 342 X-1	0093640901†	51951.06	$0.58^{+0.09}_{-0.08}$	2.01*	$1.48^{+0.04}_{-0.11}$	$0.40^{+0.05}_{-0.04}$	136/138	0.53	$0.78^{+0.13}_{-0.12}$	$2.56^{+0.08}_{-0.08}$	$3.80^{+0.12}_{-0.12}$	$0.89^{+0.04}_{-0.04}$	0.59 ± 0.02	0.14 ± 0.01	19.94 ± 2.78	6.24 ± 0.63
($d = 3.61$ Mpc)	0206890101†	53055.31	$0.71^{+0.02}_{-0.02}$	$2.19^{+0.22}_{-0.16}$	$1.86^{+0.03}_{-0.03}$	–	282/305	0.82	–	$3.62^{+0.09}_{-0.09}$	$10.73^{+0.17}_{-0.17}$	–	1.67 ± 0.03	–	13.11 ± 0.79	2.94 ± 0.14
	0206890201†	53234.82	$0.74^{+0.07}_{-0.07}$	$2.98^{+1.56}_{-0.61}$	$1.74^{+0.06}_{-0.09}$	$0.30^{+0.02}_{-0.02}$	287/275	0.29	$1.28^{+0.06}_{-0.06}$	$3.49^{+0.06}_{-0.06}$	$5.83^{+0.12}_{-0.12}$	$1.68^{+0.05}_{-0.05}$	0.91 ± 0.02	0.26 ± 0.01	12.23 ± 3.69	3.48 ± 0.57
	0 693 850 601	56150.83	$0.78^{+0.08}_{-0.07}$	$2.51^{+0.31}_{-0.23}$	$1.70^{+0.06}_{-0.07}$	$0.24^{+0.02}_{-0.01}$	336/361	0.82	$1.82^{+0.08}_{-0.08}$	$3.45^{+0.06}_{-0.06}$	$6.59^{+0.09}_{-0.09}$	$2.55^{+0.07}_{-0.07}$	1.03 ± 0.01	0.40 ± 0.01	13.94 ± 1.31	3.81 ± 0.50
	0693851301†	56156.84	$0.68^{+0.06}_{-0.05}$	$2.79^{+0.52}_{-0.35}$	$1.82^{+0.05}_{-0.03}$	$0.28^{+0.02}_{-0.02}$	394/376	0.25	$0.83^{+0.05}_{-0.04}$	$4.46^{+0.04}_{-0.04}$	$6.32^{+0.05}_{-0.05}$	$1.11^{+0.06}_{-0.06}$	0.99 ± 0.08	0.17 ± 0.01	11.84 ± 1.32	3.06 ± 0.26

Notes. †Non-detection of QPO.
*Frozen parameter value.
⊠$P_{null} < 0.1$ yielded due to excess residuals at 0.56 and 1 keV in some of the observations of NGC 1313 X−1 and NGC 5408 X−1.

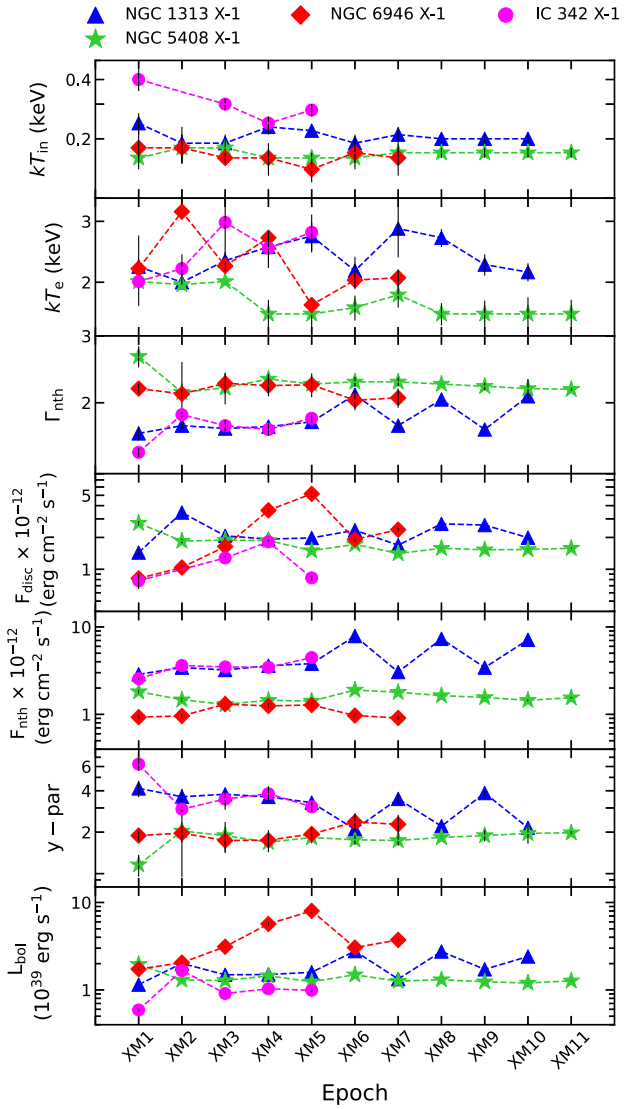

Figure 5. Long-term evolution of the spectral parameters obtained from the best fitted energy spectra of all the sources using model M2. From top to bottom panels, the variation of disc temperature (kT_{in}), electron temperature (kT_e), photon index (Γ_{nth}), disc flux (F_{disc}), Comptonization flux (F_{nth}), Compton y-parameter (y-par), and bolometric luminosity (L_{bol}) are depicted at different epochs. Filled points, namely triangle (blue), diamond (red), circle (magenta), and asterisk (green) joined with dashed lines denote results for NGC 1313 X−1, NGC 6946 X−1, IC 342 X−1, and NGC 5408 X−1, respectively. See the text for details.

to the observations of epoch XM5 to XM8 (See Table 1) during which the source shows a purely disc-dominated spectral state (see Fig. 5). The estimated values of these constants are obtained in the range of $1.87 < A < 21.38$ and $2.86 < C < 40.56$, respectively for all the sources as indicated in Fig. 7.

6.3 Spectrotemporal correlations

Next, we examine the correlations among the spectrotemporal properties of the four BH-ULXs. We depict the obtained results in Fig. 8, where the variation of F_{nth}/F_{tot} (in per cent), F_{disc}/F_{tot} (in per cent), Γ_{nth}, and f_{scatt} with QPO rms amplitudes (rms_{QPO}) are presented from top to bottom panels, respectively. Here, F_{nth} is the

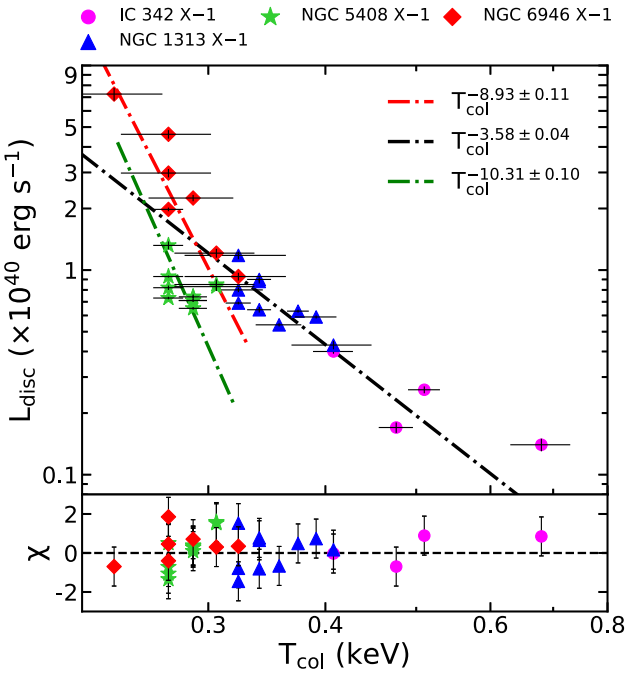

Figure 6. Variation of bolometric disc luminosity (L_{disc}) with colour corrected inner disc temperature (T_{col}) of four BH-ULXs. The results are obtained from the spectral fitting with the model M2. The filled points with different colours and styles denote various BH-ULXs as marked at the top of the figure. Dot-dashed lines represent best fitted function $L_{disc} \propto T_{col}^{\alpha}$. The blue shaded region indicates the 2σ interval of the best fit. Bottom panel denotes the variation of residuals in units of σ. See the text for details.

`nthComp` flux, F_{disc} is the `diskbb` flux, F_{tot} is the total spectral flux, and f_{scatt} denotes the scattered fraction of the seed photons. In each panel, filled points with different styles and colours denote results corresponding to different sources as marked at the top of the figure. We observe that Comptonized flux generally contributes about $50 - 90$ per cent, whereas disc flux ranges within $3 - 50$ per cent across the overall range of rms_{QPO} (per cent). However, we notice that the flux contributions for NGC 5408 X−1 seem coarsely dependent on rms_{QPO} (per cent). In addition, f_{scatt} is seen to vary in the range of $2 - 20$ per cent that eventually corroborates the signature of Comptonization of the seed photons. Further, the photon index (Γ_{nth}) is found to vary in the range of 1.48–2.65 for all the sources. Note that NGC 6946 X−1 and NGC 5408 X−1 show relatively softer spectral characteristics ($\Gamma_{nth} \gtrsim 2$) compared to other sources ($\Gamma_{nth} \lesssim 2$) which is consistent with the variation of emission components (F_{disc} and F_{nth}) to the total flux (F_{tot}) of the sources.

Overall, all the above findings, as presented in Section 5–6, plausibly indicate that the accretion flow seems to be comprised with a hot Comptonized component resides at the vicinity of the central source, and a relatively low temperature disc confined around the disc equatorial plane. Accordingly, in the next section, we adopt a model of the relativistic, dissipative, low angular momentum accretion flow around the rotating black hole and calculate the global transonic accretion solutions containing shock wave, where hot and dense post-shock flow presumably mimic the Compton corona. Subsequently, we employ the solution of this kind to explain the observed QPO frequency and disc luminosity for a given BH-ULX, and attempt to constrain the physical parameters of the source, namely the mass, spin, and accretion rate.

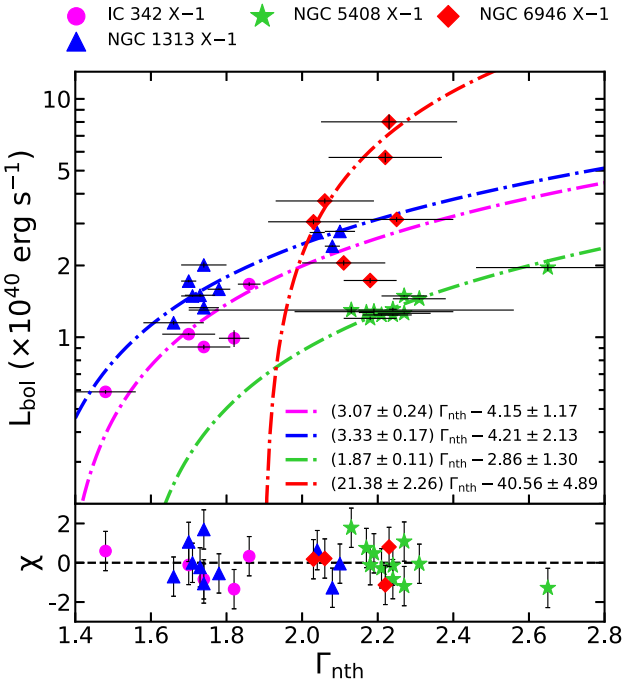

Figure 7. Variation of total bolometric luminosity (L_{bol}) with `nthComp` photon index (Γ_{nth}) for four BH-ULXs. Filled points having different colours and styles are for different sources as marked at the top of the figure. The dot-dashed curves represent the best fitted linear functions for individual sources. Bottom panel denotes the variation of residuals in units of σ. See the text for details.

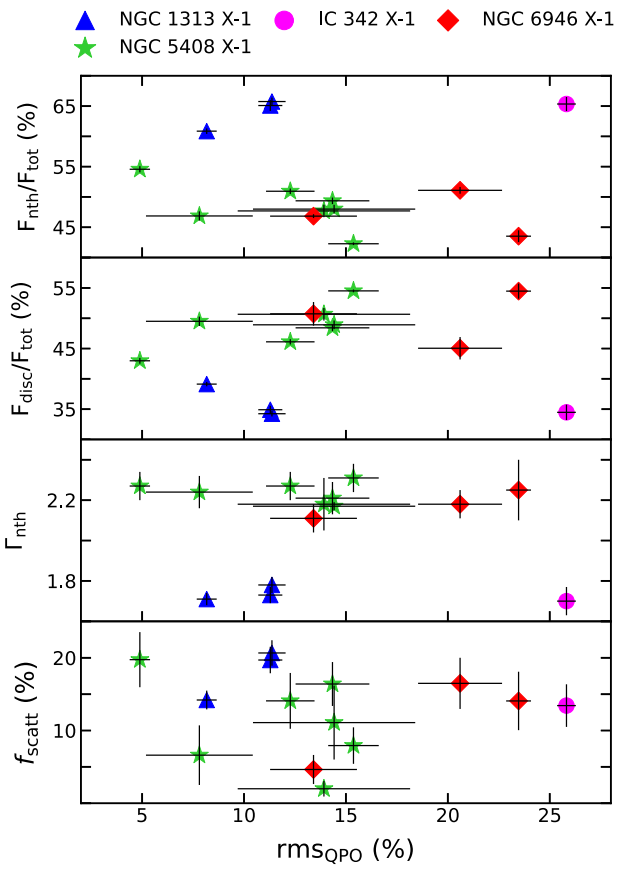

Figure 8. Variations of the percentage of Comptonized flux (F_{nth}) and disc flux (F_{disc}) to the total spectral flux (F_{tot}), `nthComp` photon index (Γ_{nth}) and scattered fraction of Comptonized seed photons (f_{scatt}) with QPO rms amplitude (rms_{QPO} (per cent)) for four BH-ULXs are depicted from top to bottom panel, respectively. Results from different BH-ULXs are presented using filled points with different styles and colours as marked at the top of the figure. See the text for details.

7 ON THE MASS, SPIN, AND ACCRETION RATE OF BH-ULXS

We utilize the observational findings of the four BH-ULXs under consideration and estimate their possible mass (M_{BH}) range in terms of the accretion rate ($\dot{m}$) and the spin (a_k) of the source. While doing so, we follow the formalism developed by Das et al. (2021) in order to study the relativistic viscous accretion flow around rotating black hole. In the work of Das et al. (2021), a model of relativistic, steady, viscous, optically thin, advective accretion flow around a ULX source is developed, where the space–time geometry around the rotating black holes is satisfactorily described using a recently formulated effective potential (Dihingia et al. 2018). With this, we solve the flow equations that govern the vertically averaged flow motion in presence of radiative coolings, namely bremsstrahlung, cyclosynchrotron, and Comptonization processes. While solving the governing equations, we adopt a closer equation in the form of relativistic equation of state to describe a thermally relativistic flow and calculate the shock induced global accretion solutions around the BH-ULXs by means of the input model parameters, namely energy ($\mathcal{E}_{in}$) and angular momentum (λ_{in}) of the flow at the inner critical point (r_{in}), mass accretion rate ($\dot{m}$), mass (M_{BH}), and spin (a_k), respectively. Using the shock properties, i.e. shock location (r_s) and post-shock velocity (u), we pragmatically calculate the QPO frequency as $\nu_{QPO} \sim t_{infall}^{-1}$, where $t_{infall} = \int_{r_s}^{r_i} u^{-1} dr$, r_i being the inner edge of the disc (Molteni, Sponholz & Chakrabarti 1996; Aktar, Das & Nandi 2015; Das et al. 2021, and references therein). In addition, we also calculate the disc luminosity corresponding to the shocked accretion solutions as $L = 4\pi \int_{r_f}^{r_i} \mathcal{G} Q r H dr$, where r_f is the outer edge of the disc, Q is the total cooling rates, H is the local disc half-thickness, and $\mathcal{G}$ ($\approx 1 - \frac{2r}{r^2+a_k^2}$) denotes the gravitational redshift factor (Das et al. 2021). In this work, total cooling (Q) involves bremsstrahlung, cyclosynchrotron, and comptonization processes (Mandal & Chakrabarti 2005).

Using the input model parameters, namely $\mathcal{E}_{in}$ and λ_{in}, we compute the shock induced global accretion solutions for a given set of ($\dot{m}$, M_{BH}, a_k), that provide the observed ν_{QPO} and L_{bol} of the BH-ULX sources. Here, we choose viscosity as $\alpha = 0.01$ for the purpose of representation. Subsequently, by tuning $\mathcal{E}_{in}$ and λ_{in}, we calculate the maximum observed QPO frequency (ν_{QPO}^{max}, see Table 2) and the corresponding luminosity (L_{bol}, see Table 4) of the given BH-ULX source. Here, we consider ν_{QPO}^{max} as a reference frequency to corroborate the theoretical model prediction. Needless to mention that other observed QPO frequencies can also be explained with the adopted model (see Appendix C). The obtained results are presented in Fig. 9, where the correlation between the accretion rate ($\dot{m}$) and the mass (M_{BH}) of a given BH-ULXs is depicted as function of a_k. In each panel, regions shaded with orange and cyan colours denote the results computed for $a_k = 0$ and 0.99, respectively. Using these results, we obtain the empirical functional form $M_{BH} = (C_0 - C_1 a_k - C_2 a_k^2)\ \dot{m}^{-3/4}$, which is found to vary as seemingly exponential with $\dot{m}$ denoted by the dashed curves. Note that the coefficients C_0, C_1, and C_2 are source specific and their values depend on a_k as well (see Table 5).

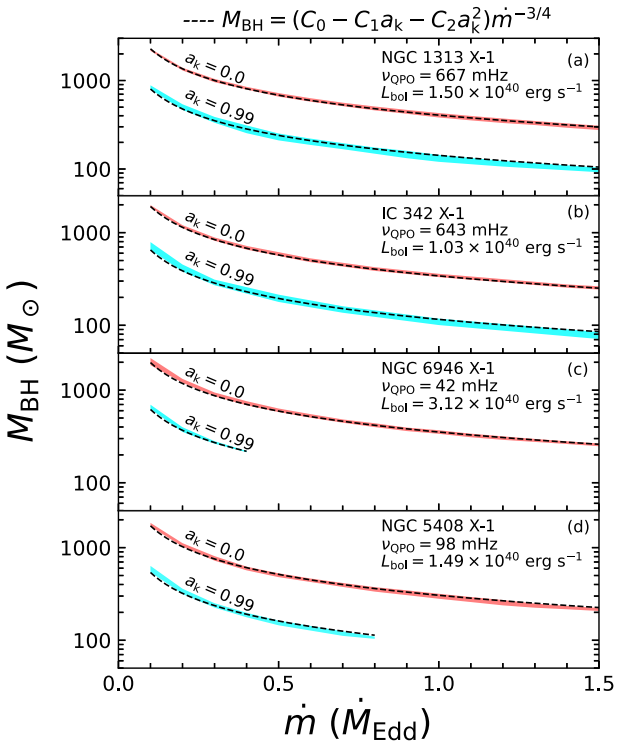

Figure 9. Correlation between mass accretion rate ($\dot{m}$) and black hole mass (M_{BH}) for different spin parameters of each source. In each panel, the regions shaded with orange and cyan indicate the mass ranges for spin parameter a_k = 0.0 and 0.99, respectively. The source details and corresponding luminosity and QPO frequency values are also mentioned in each panel. See the text for details.

In Fig. 9(a), we depict the results for NGC 1313 X−1, where $\nu_{QPO}^{max} = 667$ mHz and $L_{bol} = 1.50 \times 10^{40}$ erg s^{-1} are considered. With this, we find that the source NGC 1313 X−1 can accrete at both sub- and super-Eddington accretion rate ($0.1 \leq \dot{m} \leq 1.5$). Considering its limiting spin values, we compute the mass range of the central source which is obtained as $275 \lesssim (M_{BH}/M_\odot) \lesssim 2283$ for $a_k = 0$, and $92 \lesssim (M_{BH}/M_\odot) \lesssim 883$ for $a_k = 0.99$, respectively (see Table 5). Furthermore, we also attempt to explain the observed ν_{QPO} (∼305 and ∼82 mHz) and the corresponding L_{bol} (∼1.59×10^{40} and ∼1.49×10^{40} erg s^{-1}) of this source using our theoretical model and present the obtained results in Appendix C.

We present the results for IC 342 X−1 in Fig. 9(b). For this source, we obtain maximum QPO frequency as $\nu_{QPO}^{max} = 643$ mHz and the corresponding luminosity as $L_{bol} = 1.03 \times 10^{40}$ erg s^{-1}. We observe that the BH-ULX source IC 342 X−1 may accrete at both sub- and super-Eddington accretion rate ($\dot{m}$) irrespective to its spin value (a_k). Given that the mass of the central source (M_{BH}) is initially seen to decrease rapidly with $\dot{m}$ and then gradually tends to follow its asymptotic value for larger $\dot{m}$. In particular, for $0.1 \leq \dot{m} \leq 1.5$, we obtain $255 \lesssim (M_{BH}/M_\odot) \lesssim 1985$ when $a_k = 0$, and $71 \lesssim (M_{BH}/M_\odot) \lesssim 791$ for $a_k = 0.99$, respectively (see Table 5).

In case of NGC 6946 X−1, we consider $\nu_{QPO}^{max} = 42$ Hz and $L_{bol} = 3.12 \times 10^{40}$ erg s^{-1} and obtain the $\dot{m} - M_{BH}$ correlation by means of the source spin (a_k). The obtained results are presented in Fig. 9(c), where we observe that the central source accretes at sub-Eddington accretion rate only ($\dot{m} \lesssim 0.4$) when $a_k \to 1$. On contrary, the source can accrete at both sub- and super-Eddington accretion rate provided the central source is weakly rotating ($a_k \to 0$). Considering this, we obtain the limiting range of the source mass and the results are obtained as $248 \lesssim (M_{BH}/M_\odot) \lesssim 2221$ when $a_k = 0$, and $214 \lesssim (M_{BH}/M_\odot) \lesssim 696$ for $a_k = 0.99$, respectively (see Table 5).

For NGC 5480 X−1, we choose $\nu_{QPO}^{max} = 98$ Hz and $L_{bol} = 1.49 \times 10^{40}$ erg s^{-1} and compute $\dot{m} - M_{BH}$ correlation in terms of the spin parameter (a_k). The results are shown in Fig. 9(d), where we find that the central source accretes at sub-Eddington accretion rate ($\dot{m} \lesssim 0.8$), provided it is rapidly rotating ($a_k \to 1$). However, if the central source is weakly rotating ($a_k \to 0$), it may accrete at both sub- and super-Eddington accretion rate. For this source, the mass range is calculated as $207 \lesssim (M_{BH}/M_\odot) \lesssim 1851$ when $a_k = 0$, and $104 \lesssim (M_{BH}/M_\odot) \lesssim 635$ for $a_k = 0.99$, respectively (see Table 5).

8 DISCUSSION AND CONCLUSIONS

In this work, we carry out a comprehensive spectrotemporal analysis of five BH-ULXs that exhibit QPO features observed with *XMM–Newton*. This study allows us to investigate the accretion dynamics of the ULX sources as well as the nature of the central engine.

With this, we examine the short-term variability of the ULXs and find that the fractional variability (F_{var}) of 200 s binned light curves vary in the range of 1.42–27.28 per cent. Similar variability properties are also observed for IC 342 X−1 and NGC 5408 X−1 (see also Pintore et al. 2014). Here, we mention that NGC 6946 X−1 is found to be the most variable source with $F_{var} \sim 27$ per cent. While computing the HID of the ULXs, we find that the count rate generally increases with HID for all sources under consideration except IC 342 X−1, where source intensity is seen to vary significantly although HID varies marginally.

We perform the power spectral analysis of all five BH-ULXs and confirm the existence of QPO signatures in the frequency range 8.44–643.40 mHz in all sources (see also Atapin et al. 2019; Fabrika et al. 2021, and references therein). In addition, for NGC 5408 X−1, we find an additional significant ($\sigma \sim 2.73$) QPO feature of frequency ∼98 mHz appeared simultaneously along with ∼38 mHz QPO frequency (see Table 2 and Fig. 2). The rms amplitude and significance of the QPOs for all the sources are seen to vary in the range of 4.25–29.05 per cent and 1.62–9.41σ, respectively (see Table 2). We further mention that all five BH-ULXs are found to manifest QPO features irrespective to the hardness ratio in the range of 0.05–1.40, although the similar QPO features are generally observed from BH-XRBs in their hard and intermediate states (Remillard & McClintock 2006).

We carry out comprehensive spectral analysis by incorporating several phenomenological and physical models while modelling the combined *EPIC-PN* and *EPIC-MOS* spectra of *XMM–Newton* in 0.3–10 keV energy range (see Section 5 for details). We find that the phenomenological model combination (model M1) consisting of two disc components (`diskbb`) along with a Comptonization component (`simpl`) satisfactorily describes the observed spectra. Indeed, the model M1 elucidates the spectra in terms of relatively hotter as well as softer standard disc components with temperatures varying in the range of 0.75–3.13 keV and 0.16–0.60 keV, respectively. The scattered fraction (f_{scatt}) is found to vary in a wide range of 1.99–60.64 per cent (see Table 3), that suggests significant Comptonization of the seed photons originated from the disc. Similar model formalism involving standard and slim discs is used to explain the spectral features of NGC 1313 X−1 (Walton et al. 2020).

Next, we explore a physical model (model M2) by combining `nthComp` and `diskbb` components, and it satisfactorily describes the observed spectra of four BH-ULXs. The best-fitting model spectra of these sources result the ranges of `nthComp` photon

Table 5. Coefficients of the fitted functional form $M_{\rm BH} = (C_0 - C_1 a_{\rm k} - C_2 a_{\rm k}^2)\, \dot{m}^{-3/4}$ along with the black hole mass and accretion rate correlation for spin parameter $a_{\rm k} = 0.0$ and 0.99. The obtained mass and accretion rate ranges are also tabulated for each source.

Source	$\nu_{\rm QPO}^{\rm max}$ (mHz)	$L_{\rm bol}$ (10^{40} erg s^{-1})	$a_{\rm k} = 0$			$a_{\rm k} = 0.99$				
			C_0	$M_{\rm BH}$ ($M_\odot$)	Remarks	C_0	C_1	C_2	$M_{\rm BH}$ ($M_\odot$)	Remarks
NGC 1313 X−1	667	1.50	405.73	275–2283	$\dot{m} \lessgtr \dot{M}_{\rm Edd}$	352.73	31.83	182.32	92–883	$\dot{m} \lessgtr \dot{M}_{\rm Edd}$
IC 342 X−1	643	1.03	340.82	255–1985	$\dot{m} \lessgtr \dot{M}_{\rm Edd}$	336.78	54.72	170.36	71–791	$\dot{m} \lessgtr \dot{M}_{\rm Edd}$
NGC 6946 X−1	42	3.12	352.72	248–2221	$\dot{m} \lessgtr \dot{M}_{\rm Edd}$	325.72	37.51	182.24	214–696	$\dot{m} < \dot{M}_{\rm Edd}$
NGC 5408 X−1	98	1.49	305.61	207–1851	$\dot{m} \lessgtr \dot{M}_{\rm Edd}$	315.54	28.62	195.21	104–635	$\dot{m} < \dot{M}_{\rm Edd}$

Note. $M_\odot$ refers the solar mass, and $\dot{M}_{\rm Edd}$ denotes the Eddington accretion rate.

index as $\Gamma_{\rm nth} = 1.48$–2.65, electron temperature as $kT_{\rm e} = 1.62$–3.76 keV, and inner disc temperature $kT_{\rm in} = 0.14^{+0.03}_{-0.02} - 0.54^{+0.15}_{-0.06}$ keV, respectively. These findings are consistent with the spectral study ($\Gamma_{\rm nth} \sim 2$, $kT_{\rm e} \sim 3.5$ keV) of two ULXs in the galaxy NGC 925 (see Pintore et al. 2018). We obtain the optical depth and Compton y-parameter values in the range of 7.65–19.94 and 1.16–6.24 that infer the existence of an optically thick medium surrounding the sources. Such a scenario of cool and optically thick accretion disc around ULXs is discussed in Gladstone et al. (2009), Pintore et al. (2018), and Kobayashi, Nakazawa & Makishima (2019). In addition, we calculate the bolometric luminosity ($L_{\rm bol}$) of four BH-ULXs using model M2 and find that $L_{\rm bol} = (0.59$–$9.34) \times 10^{40}$ erg s^{-1}. Note that $L_{\rm bol}$ remains consistent regardless the choice of different model combinations.

We also observe that the correlation between disc luminosity ($L_{\rm disc}$) and colour corrected inner disc temperature ($T_{\rm col}$) can be described as $L_{\rm disc} \propto T_{\rm col}^{\alpha}$ with negative exponent (α) for all the sources (see Section 6 and Fig. 6). These findings are in contrast as the standard accretion disc theory (Shakura & Sunyaev 1973) yields $L_{\rm disc} \propto T_{\rm col}^{4}$. Note that Kajava & Poutanen (2009) reported similar anticorrelation between $L_{\rm disc}$ and $T_{\rm col}$ considering number of ULXs including NGC 5408 X−1 and NGC 1313 X−1 and obtained similar power-law index ($\alpha \sim -3.5$) as compared to the present results ($\alpha \sim -3.58$). In addition, the source NGC 6946 X−1 and NGC 5408 X−1 render $\alpha \sim -8.93$ and -10.31, respectively (see Fig. 6). Similar findings of both positive and negative correlations between $L_{\rm disc}$ and $T_{\rm col}$ for ULXs are reported in Feng & Kaaret (2009) and Brightman et al. (2020). In explaining the anticorrelation, it is suggested that one can interpret the observed spectra in terms of outflow mechanism. The outflowing matter may enhance the luminosity along the line of sight, resulting an increase in column density also (Kajava & Poutanen 2009). However, we find no or very weak correlation (anticorrelation) between column density and luminosity (temperature). We also find positive correlations between $L_{\rm bol}$ and $\Gamma_{\rm nth}$ for all four BH-ULXs that eventually indicates the softening of the observed spectra with the increase of $L_{\rm bol}$. Such correlations are satisfactorily explained using the liner relationship between $L_{\rm bol}$ and $\Gamma_{\rm nth}$ (see Fig. 7) as is generally seen in several BH-XRBs and ULXs (Kajava & Poutanen 2009).

Further, we explore the spectrotemporal correlations for all four BH-ULXs. We find that the Comptonized emission dominates ($F_{\rm nth} \sim 50 - 90$ per cent $F_{\rm tot}$) over the disc emission ($F_{\rm disc} \sim 50$ per cent $F_{\rm tot}$) up to 15 per cent $rms_{\rm QPO}$, whereas both disc and Comptonized emissions contribute almost similarly for $rms_{\rm QPO} > 15$ per cent. In addition, the scattered fraction ($f_{\rm scatt}$) of the seed photons via Comptonization is found to be in the range of $\sim 10 - 20$ per cent irrespective to $rms_{\rm QPO}$ values except few observations where $f_{\rm scatt} < 10$ per cent. We also observe that `nthComp` belongs to intermediate range as ∼1.5–2.3. Based on the above findings, we infer that the effect of Comptonization (Sreehari et al. 2020; Gill et al. 2021; García et al. 2022; Majumder et al. 2022; Cao et al. 2023; Peirano et al. 2023; Titarchuk & Seifina 2023; Zhang et al. 2023; and references therein for BH sources) plays a viable role in regulating the accretion dynamics around BH-ULXs.

Meanwhile, a number of models have been put forward to explain the nature of the ULXs from theoretical front. Poutanen et al. (2007) suggested a supercritical accretion model for ULXs, accounting the effects of advection and outflow. A good agreement between the derived luminosity–temperature relation with the observations is seen with this model. In addition, the effects of partially inhomogeneous wind in spectrotemporal variability of ULXs is also discussed extensively (Middleton et al. 2015). However, the model is found to be dependent on inclination angle and mass accretion rate. Further, Ambrosi et al. (2022) pointed out that the super-Eddington accretion onto black holes of masses in the range of 35–55$M_\odot$ with mass ejection scenario is congruous with the properties of the ULXs. Alternatively, Narayan, Sa̧dowski & Soria (2017) proposed a model based on the general relativistic magnetohydrodynamic simulation for a stellar mass black hole accreting at super-Eddington rate. Indeed, depending on the mass accretion rate, black hole spin, inclination angle, and magnetic field configuration, the model yields a luminosity above $\sim 10^{40}$ erg s^{-1}. In addition, Mondal & Mukhopadhyay (2019) proposed an advective magnetized accretion-ejection mechanism around a stellar mass black hole that explains the observational aspects of ULXs in power-law dominated state. Recently, Das et al. (2021) developed a physically motivated model by incorporating the relativistic dissipative accretion flow in ULXs. Adopting this model formalism, it is found that accretion in both massive stellar-mass and intermediate mass black holes can power the ULX sources, depending on their mass accretion rate and the spin values (see Fig. 9 and Table 5). In particular, we observe that NGC 6946 X−1 and NGC 5408 X−1 possibly accrete at sub-Eddington rate provided their central sources are rapidly rotating ($a_{\rm k} \to 1$). On contrary, IC 342 X−1 and NGC 1313 X−1 seems to accrete either at sub- or super-Eddington accretion rate depending on the spin values ($0 \leq a_{\rm k} \leq 0.99$) of the central accretor.

Finally, we mention the limitation of this work. In our analysis, we consider that the ULX sources under consideration harbour black hole at their central core. However, the nature of the central source in ULXs could be neutron star as well even with no detection of pulsed emission (King et al. 2017; Walton et al. 2018b). Hence, we indicate that the overall conclusions delineated in this work are subjected to alter for neutron star accretors as the inner boundary conditions for neutron star accretion differ from black hole system (Frank, King & Raine 2002). This aspect is indeed relevant, however its implementation is beyond the scope of this work, which we plan to take up as future work.

ACKNOWLEDGEMENTS

Authors thank the anonymous reviewer for constructive comments and useful suggestions that helped us to improve the quality of the manuscript. SD thanks Science and Engineering Research Board (SERB), India for support under grant MTR/2020/000331. SM and SD also thank the Department of Physics, IIT Guwahati, India for providing the facilities to complete this work. VKA and AN thank GH, SAG; DD, PDMSA, and Director, URSC for encouragement and continuous support to carry out this research. This publication uses the data from the *XMM-Newton* mission, archived at the HEASARC data centre. The instrument team is thanked for processing and providing the useful data as well as software for this analysis.

DATA AVAILABILITY

Data used for this publication are currently available at the HEASARC browse website (https://heasarc.gsfc.nasa.gov/db-perl/W3Browse/w3browse.pl).

REFERENCES

Abramowicz M. A., Czerny B., Lasota J. P., Szuszkiewicz E., 1988, ApJ, 332, 646
Agrawal V. K., Nandi A., 2015, MNRAS, 446, 3926
Aktar R., Das S., Nandi A., 2015, MNRAS, 453, 3414
Ambrosi E., Zampieri L., Pintore F., Wolter A., 2022, MNRAS, 509, 4694
Anand G. S., Rizzi L., Tully R. B., 2018, AJ, 156, 105
Arnaud K. A., 1996, in Jacoby G. H., Barnes J.eds, ASP Conf. Ser. Vol. 101, Astronomical Data Analysis Software and Systems V. Astron. Soc. Pac., San Francisco, p. 17
Atapin K., Fabrika S., Caballero-García M. D., 2019, MNRAS, 486, 2766
Bachetti M. et al., 2013, ApJ, 778, 163
Bachetti M. et al., 2014, Nature, 514, 202
Belloni T., Homan J., Casella P., van der Klis M., Nespoli E., Lewin W. H. G., Miller J. M., Méndez M., 2005, A&A, 440, 207
Belloni T. M., Sanna A., Méndez M., 2012, MNRAS, 426, 1701
Bhuvana G. R., Radhika D., Agrawal V. K., Mandal S., Nandi A., 2021, MNRAS, 501, 5457
Bregman J. N., Cox C. V., Tomisaka K., 1993, ApJ, 415, L79
Brightman M. et al., 2016a, ApJ, 816, 60
Brightman M. et al., 2016b, ApJ, 829, 28
Brightman M. et al., 2019, ApJ, 873, 115
Brightman M., Walton D. J., Xu Y., Earnshaw H. P., Harrison F. A., Stern D., Barret D., 2020, ApJ, 889, 71
Caballero-García M. D., Fabian A. C., 2010, MNRAS, 402, 2559
Caballero-García M. D., Belloni T., Zampieri L., 2013, MNRAS, 436, 3262
Cao Z., Jonker P. G., Wen S., Stone N. C., Zabludoff A. I., 2023, MNRAS, 519, 2375
Carpano S., Haberl F., Maitra C., Vasilopoulos G., 2018, MNRAS, 476, L45
Colbert E. J. M., Mushotzky R. F., 1999, ApJ, 519, 89
Cseh D., Grisé F., Kaaret P., Corbel S., Scaringi S., Groot P., Falcke H., Körding E., 2013, MNRAS, 435, 2896
Das S., Nandi A., Agrawal V. K., Dihingia I. K., Majumder S., 2021, MNRAS, 507, 2777
De Marco B., Ponti G., Miniutti G., Belloni T., Cappi M., Dadina M., Muñoz-Darias T., 2013, MNRAS, 436, 3782
Dewangan G. C., Titarchuk L., Griffiths R. E., 2006, ApJ, 637, L21
Dihingia I. K., Das S., Maity D., Chakrabarti S., 2018, Phys. Rev. D, 98, 083004
Done C., Davis S. W., 2008, ApJ, 683, 389
Earnshaw H. P. et al., 2019, ApJ, 881, 38
Ebisawa K., Życki P., Kubota A., Mizuno T., Watarai K.-Y., 2003, Chin. J. Astron. Astrophys. Suppl., 3, 415
Edelson R., Turner T. J., Pounds K., Vaughan S., Markowitz A., Marshall H., Dobbie P., Warwick R., 2002, ApJ, 568, 610
Fabbiano G., 1989, ARA&A, 27, 87
Fabbiano G., Trinchieri G., 1987, ApJ, 315, 46
Fabrika S., Mescheryakov A., 2001, in Schilizzi R. T.ed., Galaxies and their Constituents at the Highest Angular Resolutions, Vol. 205. Cambridge Univ. Press, Cambridge, p. 268
Fabrika S. N., Atapin K. E., Vinokurov A. S., Sholukhova O. N., 2021, Astrophys. Bull., 76, 6
Feng H., Kaaret P., 2005, ApJ, 633, 1052
Feng H., Kaaret P., 2007, ApJ, 668, 941
Feng H., Kaaret P., 2009, ApJ, 696, 1712
Feng H., Soria R., 2011, New Astron. Rev., 55, 166
Feng H., Rao F., Kaaret P., 2010, ApJ, 710, L137
Frank J., King A., Raine D. J., 2002, Accretion Power in Astrophysics: Third Edition. Cambridge Univ. Press, Cambridge, UK
Fürst F. et al., 2016, ApJ, 831, L14
García F., Karpouzas K., Méndez M., Zhang L., Zhang Y., Belloni T., Altamirano D., 2022, MNRAS, 513, 4196
Ghosh T., Rana V., 2021, MNRAS, 504, 974
Ghosh T., Rana V., Bachetti M., 2022, ApJ, 938, 76
Gill R., Sonbas E., Dhuga K. S., Gogus E., 2021, preprint (arXiv:2111.13316)
Gladstone J. C., Roberts T. P., Done C., 2009, MNRAS, 397, 1836
Goodman J., Weare J., 2010, Commun. Appl. Math. Comput. Sci., 5, 65
Gúrpide A., Godet O., Koliopanos F., Webb N., Olive J. F., 2021, A&A, 649, A104
Heil L. M., Vaughan S., 2010, MNRAS, 405, L86
Hernández-García L., Vaughan S., Roberts T. P., Middleton M., 2015, MNRAS, 453, 2877
Hirano A., Kitamoto S., Yamada T. T., Mineshige S., Fukue J., 1995, ApJ, 446, 350
Hua X.-M., Titarchuk L., 1995, ApJ, 449, 188
Huang C. Y., 2019, Contrib. Astron. Obs. Skalnate Pleso, 49, 7
Israel G. L. et al., 2017, Science, 355, 817
Jansen F. et al., 2001, A&A, 365, L1
Jithesh V., Misra R., Wang Z., 2017, ApJ, 849, 121
Kaaret P., Feng H., Roberts T. P., 2017, ARA&A, 55, 303
Kajava J. J. E., Poutanen J., 2009, MNRAS, 398, 1450
Kara E. et al., 2020, MNRAS, 491, 5172
King A. R., 2002, MNRAS, 335, L13
King A., Lasota J.-P., Kluźniak W., 2017, MNRAS, 468, L59
Kobayashi S. B., Nakazawa K., Makishima K., 2019, MNRAS, 489, 366
Kubota A., Makishima K., 2004, ApJ, 601, 428
Kubota A., Mizuno T., Makishima K., Fukazawa Y., Kotoku J., Ohnishi T., Tashiro M., 2001, ApJ, 547, L119
Leahy D. A., Darbro W., Elsner R. F., Weisskopf M. C., Sutherland P. G., Kahn S., Grindlay J. E., 1983, ApJ, 266, 160
Luangtip W., Chainakun P., Loekkesee S., Deesamer C., Ngonsamrong T., Sintusiri T., 2021, MNRAS, 507, 6094
Majumder S., Sreehari H., Aftab N., Katoch T., Das S., Nandi A., 2022, MNRAS 512 2508
Makishima K., Maejima Y., Mitsuda K., Bradt H. V., Remillard R. A., Tuohy I. R., Hoshi R., Nakagawa M., 1986, ApJ, 308, 635
Makishima K. et al., 2000, ApJ, 535, 632
Mandal S., Chakrabarti S. K., 2005, A&A, 434, 839
Marlowe H. et al., 2014, MNRAS, 444, 642
Middleton M. J., Roberts T. P., Done C., Jackson F. E., 2011, MNRAS, 411, 644
Middleton M. J., Heil L., Pintore F., Walton D. J., Roberts T. P., 2015, MNRAS, 447, 3243
Miller J. M., Fabbiano G., Miller M. C., Fabian A. C., 2003, ApJ, 585, L37
Mineshige S., Hirano A., Kitamoto S., Yamada T. T., Fukue J., 1994, ApJ, 426, 308
Miyawaki R., Sugiho M., Kubota A., Makishima K., Namiki M., Tanaka T., Tsunoda N., 2006, in Wilson A.ed., ESA Special Publication, Vol. 604, The X-ray Universe 2005. ESA, Madrid, p. 433
Molteni D., Sponholz H., Chakrabarti S. K., 1996, ApJ, 457, 805
Mondal T., Mukhopadhyay B., 2019, MNRAS, 482, L24
Mukherjee E. S. et al., 2015, ApJ, 808, 64
Nandi A., Debnath D., Mandal S., Chakrabarti S. K., 2012, A&A, 542, A56

Narayan R., Sa̧dowski A., Soria R., 2017, MNRAS, 469, 2997
Pasham D. R., Strohmayer T. E., 2012, ApJ, 753, 139
Pasham D. R., Strohmayer T. E., Mushotzky R. F., 2014, Nature, 513, 74
Pasham D. R., Cenko S. B., Zoghbi A., Mushotzky R. F., Miller J., Tombesi F., 2015, ApJ, 811, L11
Peirano V., Méndez M., García F., Belloni T., 2023, MNRAS, 519, 1336
Pintore F., Zampieri L., 2012, MNRAS, 420, 1107
Pintore F., Zampieri L., Wolter A., Belloni T., 2014, MNRAS, 439, 3461
Pintore F. et al., 2018, MNRAS, 479, 4271
Poutanen J., Lipunova G., Fabrika S., Butkevich A. G., Abolmasov P., 2007, MNRAS, 377, 1187
Quintin E., Webb N. A., Gúrpide A., Bachetti M., Fürst F., 2021, MNRAS, 503, 5485
Rao F., Feng H., Kaaret P., 2010, ApJ, 722, 620
Remillard R. A., McClintock J. E., 2006, ARA&A, 44, 49
Reynolds C. S., Loan A. J., Fabian A. C., Makishima K., Brandt W. N., Mizuno T., 1997, MNRAS, 286, 349
Roberts T., 2007, Astrophys. Space Sci., 311, 203
Roberts T. P., Warwick R. S., 2000, MNRAS, 315, 98
Rodríguez Castillo G. A. et al., 2020, ApJ, 895, 60
Rybicki G. B., Lightman A. P., 1979, Radiative Processes in Astrophysics. Wiley, New York
Salvaggio C. et al., 2022, MNRAS, 512, 1814
Sathyaprakash R. et al., 2019, MNRAS, 488, L35
Shakura N. I., Sunyaev R. A., 1973, A&A, 500, 33
Sreehari H., Ravishankar B. T., Iyer N., Agrawal V. K., Katoch T. B., Mandal S., Nandi A., 2019, MNRAS, 487, 928
Sreehari H., Nandi A., Das S., Agrawal V. K., Mandal S., Ramadevi M. C., Katoch T., 2020, MNRAS, 499, 5891
Steiner J. F., Narayan R., McClintock J. E., Ebisawa K., 2009, PASP, 121, 1279
Stobbart A. M., Roberts T. P., Wilms J., 2006, MNRAS, 368, 397
Strohmayer T. E., 2009, ApJ, 706, L210
Strohmayer T. E., Mushotzky R. F., 2003, ApJ, 586, L61
Strohmayer T. E., Mushotzky R. F., 2009, ApJ, 703, 1386
Strohmayer T. E., Mushotzky R., 2010, AAS/High Energy Astrophysics Division #11, 27.03
Strohmayer T. E., Mushotzky R. F., Winter L., Soria R., Uttley P., Cropper M., 2007, ApJ, 660, 580
Strüder L. et al., 2001, A&A, 365, L18
Stuchlík Z., Kološ M., 2015, MNRAS, 451, 2575
Sutton A. D., Roberts T. P., Middleton M. J., 2013, MNRAS, 435, 1758
Titarchuk L., 1994, ApJ, 434, 570
Titarchuk L., Seifina E., 2023, A&A, 669, A57
Tully R. B., Courtois H. M., Sorce J. G., 2016, AJ, 152, 50
van der Klis M., 2006, in, Lewin W., van der Klis M., eds, Compact Stellar X-ray Sources, Vol. 39. Cambridge Univ. Press, Cambridge, p. 39
Vaughan S., Edelson R., Warwick R. S., Uttley P., 2003, MNRAS, 345, 1271
Vierdayanti K., Mineshige S., Ebisawa K., Kawaguchi T., 2006, PASJ, 58, 915
Walton D. J. et al., 2018a, MNRAS, 473, 4360
Walton D. J. et al., 2018b, ApJ, 856, 128
Walton D. J. et al., 2019, AAS/High Energy Astrophysics Division, 200.04
Walton D. J. et al., 2020, MNRAS, 494, 6012
Watarai K.-y., Fukue J., Takeuchi M., Mineshige S., 2000, PASJ, 52, 133
Watarai K.-y., Mizuno T., Mineshige S., 2001, ApJ, 549, L77
Wilms J., Allen A., McCray R., 2000, ApJ, 542, 914
Winter L. M., Mushotzky R. F., Reynolds C. S., 2006, ApJ, 649, 730
Zdziarski A. A., Johnson W. N., Magdziarz P., 1996, MNRAS, 283, 193
Zhang W., Papadakis I. E., Dovčiak M., Bursa M., Karas V., 2023, MNRAS, 519, 4951
Życki P. T., Done C., Smith D. A., 1999, MNRAS, 309, 561

APPENDIX A: ESTIMATION OF QPO$_{rms}$ per cent FOR M82 X−1

Since M82 X−2 is extremely variable (Brightman et al. 2016b) and M82 X−1 is located within the 5 arcsec separation of it, the effect of possible contamination cannot be ruled out. This causes the spectral analysis of M82 X−1 challenging as the obtained results could be significantly biased and hence, we refrain from spectral study of M82 X−1. However, we estimate QPO$_{rms}$ per cent as the QPO feature originates from M82 X−1 only. While estimating QPO_{rms} per cent, we make use of the nearby *Chandra* observations of M82 X-1 and M82 X-2, where we consider 3 arcsec circular region about each source and obtain the count rates of individual sources. Further, we consider 8 arcsec circular region at the centre which includes both sources (M82 X-1 and M82 X-2). Evidently, this provides the total count rates obtained from the contribution of both sources. Accordingly, the photon fraction for each source is calculated as the ratio of individual source counts to the total counts (see also Feng & Kaaret 2007; Brightman et al. 2019). We divide the estimated rms with this photon fraction of M82 X-1 and express the corrected rms in percentage. Note that Feng & Kaaret (2007) obtained the photon fraction from the 'surface brightness fit of *XMM* Image' and in this study, we estimate QPO$_{rms}$ per cent using the nearby *Chandra* observations. The details of *XMM* and *Chandra* observations (Brightman et al. 2019) along with the estimated QPO$_{rms}$ per cent are tabulated in Table A1.

Table A1. Details of M82 X−1 observations with *XMM–Newton* and *Chandra*. Corrected QPO$_{rms}$ per cent and Total$_{rms}$ per cent are presented in column 7 and 9. See the text for details.

XMM Epoch	QPO Freq. (ν_{QPO})	Estimated QPO$_{rms}$ (per cent)	*Chandra* ObsID	Date of Obs.	M82 X−1 Contribution*(per cent)	Corrected QPO$_{rms}$ (per cent)†	Estimated Total$_{rms}$ (per cent)	Corrected Total$_{rms}$ (per cent)†
XM1	$55.85^{+1.44}_{-2.01}$	4.25 ± 1.02	02933	2002-06-18	36.84	11.54 ± 4.33	12.04 ± 1.93	32.68 ± 10.30
XM2	$110.81^{+5.03}_{-4.26}$	8.35 ± 1.15	06097	2005-02-04	68.84	12.13 ± 2.18	13.91 ± 2.33	20.21 ± 4.06
XM5	$45.55^{+1.61}_{-2.19}$	5.97 ± 1.12	10545	2010-07-28	27.28	21.88 ± 7.75	18.68 ± 2.28	68.48 ± 12.84
XM6	$47.63^{+5.47}_{-3.22}$	8.99 ± 1.42	10545	2010-07-28	27.28	32.95 ± 11.18	17.63 ± 4.25	64.62 ± 24.32
XM7	$35.74^{+2.53}_{-2.44}$	7.72 ± 1.74	10545	2010-07-28	27.28	28.30 ± 10.64	11.66 ± 2.02	42.74 ± 14.28

Notes. *Contribution of M82 X−1 in the total count rate within 8 arcsec *Chandra* aperture.
†QPO$_{rms}$ per cent values involve uncertainty and hence should be referred accordingly.

APPENDIX B: FLUX AND TEMPERATURE CORRELATION

We examine whether the apparent correlation between $L_{\rm disc}$ and $T_{\rm col}$ is actually a result of degeneracy or not. In doing so, we calculate disc luminosity as $L_{\rm disc} = 4\pi d^2 F_{\rm disc}$, where $F_{\rm disc}$ is obtained from the spectral fitting with convolution model `cflux`. We compute $T_{\rm col}$ from the inner disc temperature $T_{\rm in}$ by multiplying a constant spectral hardening factor (f). Therefore, it is appropriate to perform degeneracy check between $F_{\rm disc}$ and $T_{\rm in}$ instead of $L_{\rm disc}$ and $T_{\rm col}$. We run an MCMC simulation using the Goodman-Weare algorithm (Goodman & Weare 2010) with a chain length of 20 000. The obtained results are shown in Fig. B1 for all the sources under consideration except M82 X−1. Note that $F_{\rm disc}$ depends on $T_{\rm in}$ for each source (ruling out the degeneracy between the parameters) which possibly causes the observed correlation between $L_{\rm disc}$ and $T_{\rm col}$ for the ULXs under consideration except M82 X−1.

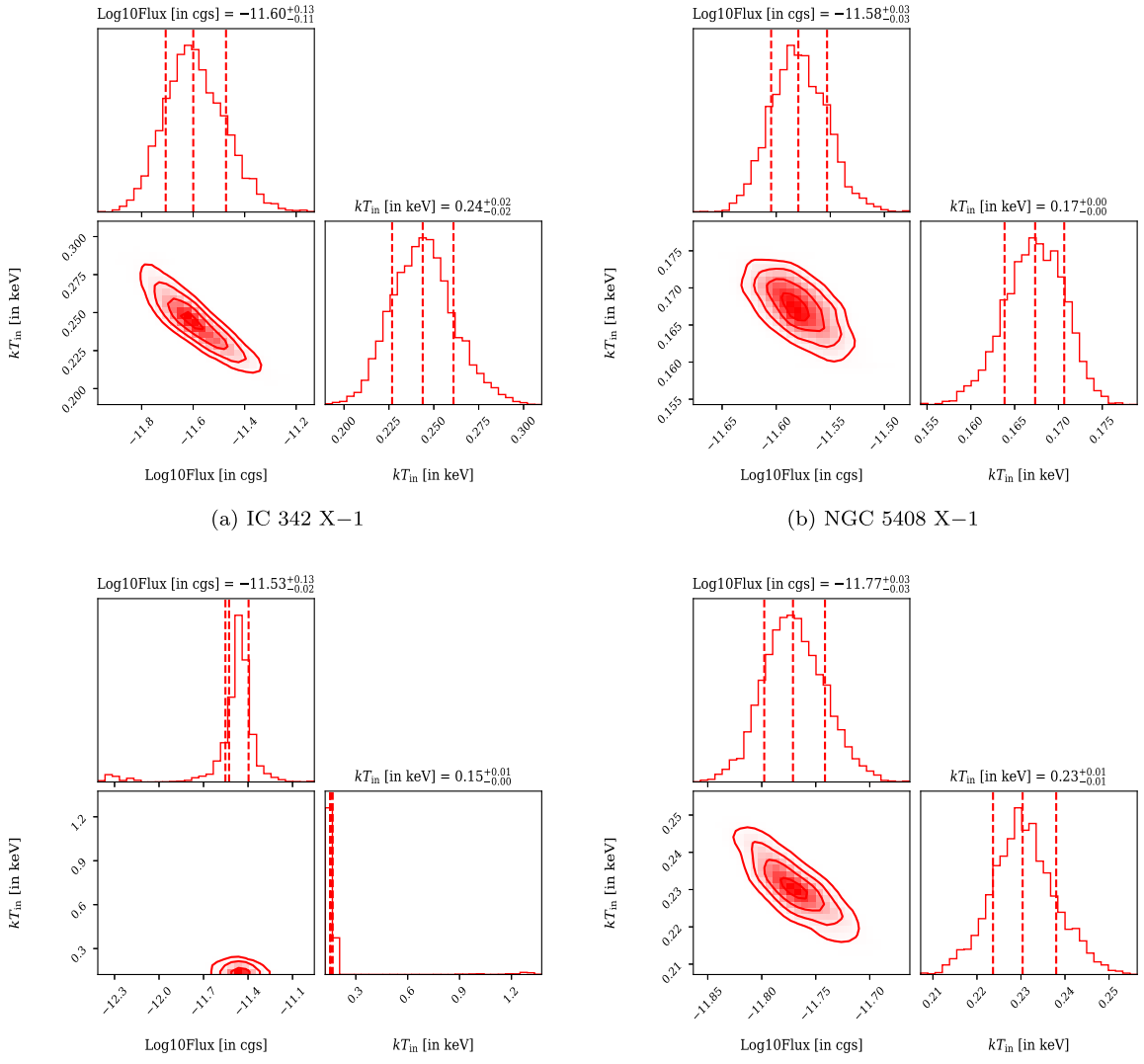

(a) IC 342 X−1 (b) NGC 5408 X−1

(c) NGC 6946 X−1 (d) NGC 1313 X−1

Figure B1. Correlation between the inner disc temperature and estimated bolometric disc flux of each source. The MCMC simulation carried out using the Goodman–Weare algorithm with a chain length of 20 000. The contours in each panel represent 1σ, 2σ, and 3σ confidence ranges.

APPENDIX C: DEPENDENCE OF $\nu_{\rm QPO}$ ON ACCRETION RATE

In order to examine how $\nu_{\rm QPO}$ and $L_{\rm bol}$ of NGC 1313 X−1 depends on the accretion rate ($\dot{m}$), we consider the mass range of the source as $958 \lesssim M_{\rm BH}/M_{\odot} \lesssim 1037$ for $a_{\rm k} = 0.0$ and $333 \lesssim M_{\rm BH}/M_{\odot} \lesssim 388$ for $a_{\rm k} = 0.99$ (see Fig. 9a). With this, we estimate the mass accretion rate in the sub-Eddington regime that satisfactorily explains both $\nu_{\rm QPO}$ and $L_{\rm bol}$. The obtained results are shown in Fig. C1. In upper (lower) panel, we choose $a_{\rm k} = 0.0$ (0.99), and solid and dashed vertical lines are for $M_{\rm BH} = 958\,M_{\odot}$ and $1037\,M_{\odot}$ ($M_{\rm BH} = 333\,M_{\odot}$ and $388\,M_{\odot}$). In both panels, the vertical lines flanked by red, blue, and green horizontal bars denote results corresponding to ($\nu_{\rm QPO}$, $L_{\rm bol}$) = (82 mHz, 1.49×10^{40} erg s^{-1}), (305 mHz, 1.59×10^{40} erg s^{-1}), and (667 mHz, 1.50×10^{40} erg s^{-1}), respectively. It is evident that $\nu_{\rm QPO}$ increases with $\dot{m}$. We further infer that similar variation of $\nu_{\rm QPO}$ with $\dot{m}$ is also very much likely in super-Eddington accretion regime as well.

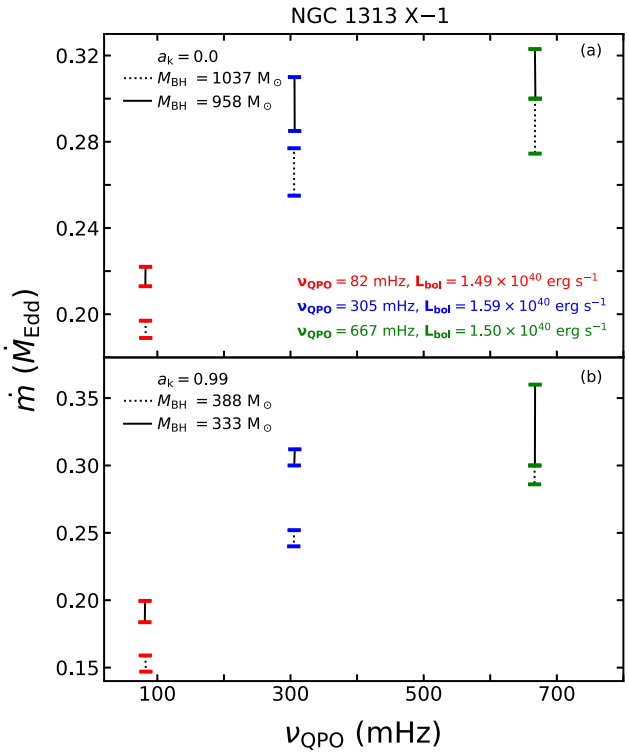

Figure C1. Variation of observed QPO frequency ($\nu_{\rm QPO}$) with model predicted accretion rate ($\dot{m}$) for NGC 1313 X−1. Results corresponding to $a_{\rm k} = 0.0$ and 0.99 are presented in panel (a) and (b), respectively. See the text for details.

This paper has been typeset from a TEX/LATEX file prepared by the author.